ORIS-Assisted SWIPT Underwater OWC System With Different Transmission Protocols

Farah Mahdi Al-Sallami, *Member, IEEE*, Yalçın Ata, *Senior Member, IEEE*, Emna Zedini, *Senior Member, IEEE*, Anna Maria Vegni, *Senior Member, IEEE*, and Sujan Rajbhandari, *Senior Member, IEEE*

***Abstract*—In Internet of Underwater Things (IoUT) scenarios, power-hungry devices need to periodically harvest energy to be alive. By dynamically controlling and redirecting the optical beam, reconfigurable intelligent surfaces (RIS) can enhance both the energy transfer and information reception processes, thereby improving the sustainability of low-power underwater devices. Simultaneous wireless information and power transfer (SWIPT) systems allows to harvest energy and receive data from the transmitted optical beam, thus feeding the low-power receiver (Rx) while downloading data. However, realistic underwater scenario can strongly affect the performance of such systems. This paper investigates the performance of ORIS-assisted SWIPT system under a realistic unified channel model for underwater optical wireless communications (OWC), considering both coherent and non-coherent detection schemes. Considering multiple attenuation losses, underwater turbulence, pointing error, and angle of arrival deviation, we derive the joint outage probability of an ORIS-aided SWIPT OWC system for different transmission protocols based on different resources that are allocated. Three approaches are investigated *i.e.*, (*i*) power-splitting (PS), (*ii*) time-switching (TS), and (*iii*) element-splitting (ES). While PS and TS are based on all-passive RIS elements, ES considers hybrid (active and passive) elements. Simulation results show enhanced performance obtained with ES approach for low signal-to-noise ratio (SNR), while PS outperforms ES for high SNR.**

***Index Terms*—Underwater wireless optical communication, turbulence, absorption, attenuation, Jerlov water, angle-of-arrival fluctuations, pointing error, simultaneous wireless information and power transfer, reconfigurable intelligent surfaces.**

I. Introduction

With the growing number of Internet of things (IoT) devices, and advanced data applications with high level task requirements such as effective computing, sensing, storing, processing, and actuation, it is needed to constantly feed low-power devices.[1] Self-power is indeed a critical requirement in IoT systems due to the diverse functionalities and widespread deployment. For instance, many IoT devices are deployed in remote or inaccessible locations (such as underwater environment) where replacing or recharging batteries is quite impractical [1], [2]. This requires the need of energy harvesting (EH) solutions to extend device lifespan without frequent maintenance [3].

Simultaneous wireless information and power transfer (SWIPT) systems are designed to overcome the external power requirements in IoT devices, while enabling data transfer simultaneously [4], [5]. By exploiting the transmitted wireless signal, SWIPT technology allows to transmit both data and power, enabling EH and information transfer (IT) simultaneously. This dual functionality ensures that IoT devices can remain operational without frequent battery replacements, making them suitable for remote or hard-to-reach locations. However, one of the main challenges SWIPT faces is severe path loss, which limits the efficiency of wireless power transfer over long distances, especially in harsh environments such as underwater. To overcome this challenge, reconfigurable intelligent surface (RIS) can be employed to significantly enhance SWIPT performance [6]. RISs are traditionally known as a planar meta-surface composed of a massive number of reflecting elements that can dynamically control the reflection, transmission, and scattering of electromagnetic waves, received from the transmitter (Tx) to the intended Rx in a controlled manner [7]. Differently from a relay node, which is not able to adaptively control and manipulate the incident beam but only to forward to the receiver, optical RISs with active elements are able to amplify and redirect the wireless signal. Specifically, the control of optical beams is provided by the RIS in terms of different transmission protocols, such as power splitting (PS), time switching (TS), and element splitting (ES). RISs can be integrated into existing networks by adjusting the communication protocols without changing hardware and standards, making them a prominent technology for future integrated terrestrial/non-terrestrial networks [8]. By

[1]https://iot-analytics.com/number-connected-iot-devices/

Received 31 October 2025; revised 3 February 2026; accepted 31 May 2026. Date of publication 9 June 2026; date of current version 29 June 2026. Dr. Sujan Rajbhandari would like to acknowledge the support provided in part by the Engineering and Physical Sciences Research Council (EPSRC) under Grant EP/Y037243/1 (TITAN Extension), and by the Marie Skłodowska-Curie Actions (MSCA) under Grant Agreement No. 101227604, Advanced Network Connectivity using Harmonious Optical and Radio Technologies. This work was supported in part by the Progetto di ricerca di rilevante interesse nazionale (PRIN) 2022 opticaL wireless under wAter positioninG for marine mOnitOriNg (LAGO-ON) Project, PNRR Missione 4, Componente 2, Investimento 1.3 Finanziato dall'Unione europea-Next Generation European Union (EU) under Grant CUP: F53D2300048. The associate editor coordinating the review of this article and approving it for publication was X. Pang. *(Corresponding author: Anna Maria Vegni.)*

Farah Mahdi Al-Sallami is with the School of Electronic and Electrical Engineering, University of Leeds, LS2 9JT Leeds, U.K. (e-mail: f.al-sallami@leeds.ac.uk).

Yalçın Ata is with the Department of Electrical and Electronics Engineering, OSTIM Technical University, OSTIM, Yenimahalle, 06374 Ankara, Türkiye, and also with SCOPT Inc., Boston, MA 02108 USA (e-mail: ylcnata@gmail.com).

Emna Zedini is with the College of Innovation and Technology, University of Michigan-Flint, Flint, MI 48502 USA (e-mail: ezedini@umich.edu).

Anna Maria Vegni is with the Department of Industrial, Electronics and Mechanical Engineering, Roma Tre University, 00146 Rome, Italy (e-mail: annamaria.vegni@uniroma3.it).

Sujan Rajbhandari is with the Institute of Photonics, University of Strathclyde, G1 1RD Glasgow, U.K. (e-mail: sujan.rajbhandari@strath.ac.uk).

Digital Object Identifier 10.1109/TCOMM.2026.3701859

© 2026 The Authors. This work is licensed under a Creative Commons Attribution 4.0 License.
For more information, see https://creativecommons.org/licenses/by/4.0/

optimizing beamforming, RISs improve signal quality, extend coverage, and mitigate path loss [9]. All these features make RISs ideal for enabling efficient EH and IT in SWIPT systems [10], [11]. It is important to note that the energy harvesting mechanism primarily targets the sustainability of low-power underwater receiver nodes and autonomous sensing platforms rather than powering the RIS itself, which may operate in passive or hybrid modes depending on deployment conditions.

Apart from RIS technology for radio frequency (RF) wireless signals, optical reconfigurable intelligent surfaces (ORISs) have been deployed in optical wireless communication (OWC) systems, including indoor visible light communication (VLC) systems [12], as well as outdoor atmospheric and underwater free space optical (FSO) links [13], [14], [15]. In underwater scenario, RIS-based technology can outperform conventional systems, both acoustic [16] and optical ones, by extending range, improving data rates, and adding functionalities like signal amplification and control [13]. Unlike RF RIS, which are based on metasurfaces, ORISs can be realized using mirror-arrays. Hence, ORISs offer several advantages for the SWIPT systems, such as improved EH as ORIS operates with very low energy consumption, making them an energy-efficient solution. Moreover, since RISs enable precise control of signal directionality, which reduces energy wastage and improves EH [17]. For SWIPT underwater systems, RISs are able to improve performance by dynamically optimizing signal reflection and mitigating channel impairments such as signal blockages and multipath fading, as well as mitigating the effects of underwater turbulence and pointing errors [18].

A. Related Works

Traditionally, acoustic communication was the dominant technology for wireless underwater communication due to their long propagation range. However, acoustic communication faces significant challenges such as low bandwidth, multipath propagation, signal attenuation, and signal distortion. To overcome these limitations, RIS technology is adopted in underwater systems. Using ray tracing techniques, Edemen et al. [19] investigated various RIS configurations for underwater wireless acoustic channel and demonstrated that RIS can extend the communication range. Similarly, Kamali et al. [20] investigate the integration of RIS in underwater acoustic communication to address reliability and performance in shallow-water and deep-water environments. Finally, in [21], Luo et al. proposed a mixed underwater RF-acoustic communication relaying system assisted by an active RIS. By virtue of their ability to retransmit and amplify signals, active elements significantly enhance the coverage and reliability of underwater communication.

Compared to underwater RF and acoustic wireless communications, underwater optical wireless communication (UOWC) technology offers a larger bandwidth, enabling Gigabit/sec data communication for tens of meters and significantly lower attenuation. However, UOWC technology requires the line-of-sight (LoS) path between a Tx and a Rx, which cannot always be guaranteed due to potential obstacle blocking the LoS path. In such scenarios, ORIS technology can be exploited to provide an alternative path. In [22], Wei et al. investigated the deployment and dynamic behavior of a RIS-equipped autonomous underwater vehicle (AUV) in a vertical single-input multiple-output UOWC system, under the influence of pointing errors. A Monte-Carlo ray tracing (MCRT) showed that RIS-assisted vertical underwater channel is characterized by Generalized-Gamma (GG) distribution.

Song et al. investigate a simultaneous transmission and reflection RIS (STAR-RIS) assisted dual-hop mixed UOWC/RF system with non-orthogonal multiple access (NOMA) [23]. In particular, a relay node employs either heterodyne detection or intensity modulated/direct detection (IM/DD) technique to process the received signal and then reformats the NOMA signal and forwards it to two land-based NOMA users via a STAR-RIS. In this paper, however, the UOWC channel is affected only by a mixture Exponential-Generalized Gamma (Exponential-Generalized Gamma (EGG)) distribution. Kumar et al. also present a hybrid RIS-assisted RF-FSO system in underwater scenario [24]. For the UOWC link, the turbulence is modeled using a GG distribution and misalignment fading is taken into account. Similarly, Naik and Chung investigated an RIS-aided UOWC system affected by underwater turbulence, beam attenuation, pointing errors and occlusion or blockage due to obstacles [13]. The authors derived closed-form expressions for bit-error-rate (BER) for binary phase shift keying (BPSK) and binary frequency shift keying (BFSK) modulation schemes for IM/DD and heterodyne detection. In [25], Gan et al. presented the performance analysis of RIS-assisted UOWC systems. However, the proposed channel model is very limited as it does not consider multiple attenuation losses. Dong et al. [26] investigated data packets forwarding and handling in an RIS-aided UOWC system. However, this work did not consider any UOWC channel model.

B. Motivation and Contributions

Differently from previous works that present mitigation techniques for turbulence-affected environments [27], [28], in this paper we exploit RIS to better overcome attenuation loss and underwater turbulence. The comprehensive literature review in the section above clearly highlights the lack of studies on RIS-assisted UOWC systems with realistic channels as many studies limit the overall UOWC channel gain without considering additive loss contributions. Moreover, only limited studies have considered ORIS-assisted SWIPT UOWC systems, highlighting the need for deeper investigation in this area. The misalignment caused by the random movement of water, as well as other features such as strong turbulence, scattering, and absorption due to underwater environments, represent the main causes of UOWC link failure. Consequently, frequent misalignment can degrade the energy harvesting capability of UOWC systems. An efficient means of overcoming these degrading factors is to recreate LoS signals and orient them to the receivers. The use of RIS in UOWC has recently been investigated, and its impact on the EH rate is a topic that needs to be deeply investigated.

To this end, we recently investigated a unified channel model for a ORIS-assisted UOWC that takes into account multiple attenuation losses such as attenuation, underwater

turbulence, pointing error, and angle-of-arrival (AOA) fluctuations. Building on this prior work and the above mentioned motivations, this paper presents the following contributions, leading to several novelties:

- Unlike our recent work [29], which adopts the GG distribution, we derive the channel model of a UOWC system using the recently introduced and experimentally verified Weibull-Generalized Gamma (WGG) distribution [30], which combines the Weibull and Generalized Gamma distributions, together with attenuation, pointing error, and AOA fluctuations. Our study differentiates from existing works in literature in terms of both addressing a WGG model for underwater medium, and investigating a SWIPT approach with different transmission protocols.
- We consider the application of SWIPT system in underwater medium, and analyze the performance with realistic environmental parameters, such as average temperature, average salinity concentration, and chlorophyll concentration of different water types.
- We derive the channel probability density function (PDF) for the proposed RIS-assisted SWIPT-UOWC system, as well as a unified PDF expression of the signal-to-noise-ratio (SNR) for coherent and non-coherent detections. These expressions are then used to derive analytical expressions of the joint outage probability (OP) for EH and IT of the proposed ORIS-assisted SWIPT-UOWC system.
- We investigate different transmission protocols for ORIS-assisted, such as PS, TS, and ES corresponding to power, time slots, and elements resources allocation of ORIS, respectively. To emphasize the role of the ORIS reflection and amplification factor, we assume PS and TS SWIPT protocols for passive elements, and ES for a combination of active and passive elements for EH and IT tasks, respectively. Numerical analysis and extensive simulations of the performance of the proposed ORIS-assisted SWIPT UOWC system have been carried out, showing the effectiveness of ES approach over PS and TS.

This paper is organized as follows. Section II presents the UOWC scenario comprised of multiple AUVs. In case of LoS blockages, connectivity links are guaranteed by the use of a ORIS-equipped AUV device. In such a scenario, the channel models are derived under the assumption of multiple additive attenuation losses, such as underwater turbulence, pointing error, and AOA fluctuations. In Section III, we present the derivations of the UOWC channel under the combination of multiple adverse channel effects. The performance metrics of the UOWC system employing either IM/DD or heterodyne methods are also provided in Section IV, followed by the asymptotic results at high SNR in Section V. Extended numerical and simulation results are carried out in Section VII, where a comparison of the results for IM/DD and heterodyne detection is presented. Finally, the conclusions are drawn in section VIII.

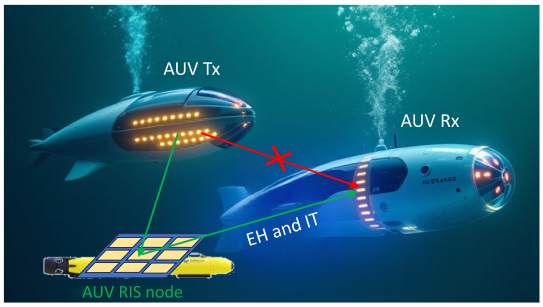

Fig. 1. Schematic of the SWIPT-UOWC system, where LoS link between the AUV Tx and AUV Rx blocked. An AUV ORIS-equipped node redirect the impinging optical signal from AUV-Tx to AUV-Rx, enabling simultaneous EH and IT.

II. System and Channel Models

A. System Model

Fig. 1 illustrates a UOWC scenario, where the LoS path between the AUV Tx and AUV Rx is blocked. To establish a connectivity between these two AUVs, an ORIS-equipped AUVs node can be employed, assuming it has unobstructed LoS path with both AUV-Tx and AUV-Rx. Notice that all devices in the underwater scenario are assumed to be at the same depth, so that the communication links are horizontal.

The ORIS includes $\mathcal{N}$ reflecting elements (with $\mathcal{N} \geq 2, \in \mathbb{N}^{+}$). We assume that the ORIS is able to redirect the irradiated optical intensity according to different protocols, such as (*i*) PS, (*ii*) TS, and (*iii*) ES, which will be described in detail in Section VI. For PS and TS protocols, the ORIS is comprised of $\mathcal{N}$ passive elements, them with a reflection coefficient $\beta_r \in (0,1)$ *i.e.*, $\beta_r \in (0,1)$, which allows the reflection of the incident optical wave by adjusting the phase and amplitude with the help of a controller. For ES protocols, the ORIS consists of $\mathcal{N}_1$ active and $\mathcal{N}_2$ passive elements (with $\mathcal{N} = \mathcal{N}_1 + \mathcal{N}_2$) for IT and EH tasks, respectively. Notice that in PS and TS protocols, all RIS elements operate in passive mode since power and time resources are already divided between EH and IT, respectively, making amplification unnecessary and energy-inefficient. Conversely, the ES protocol employs a hybrid RIS structure in which a subset of active elements amplifies the optical beam to enhance harvested energy, while passive elements maintain low-noise information reflection. This hybrid design achieves a practical trade-off between EH efficiency and system complexity under severe underwater attenuation.

B. Channel Model

Assuming an optical signal propagates in underwater medium and it is affected by turbulence, attenuation (*i.e.*, absorption and scattering), pointing error and AOA fluctuations, the combined channel state h can be defined as

$$h = h_{al} h_{pl} h_{at} h_{af}, \tag{1}$$

where h_{al}, h_{pl}, h_{at} and h_{af} illustrate the effects of attenuation, pointing error, turbulence, and AOA fluctuations, respectively. The model of each contributing phenomenon is described below.

1) Attenuation: when optical beam propagates through an underwater medium, it is severely attenuated due to combined effect of absorption and scattering. This attenuation can be described by the traditional Beer-Lambert law, *i.e.* $h_{al} = \exp[-\mathcal{C}(\lambda)L]$, where $\mathcal{C}(\lambda)$ is the attenuation coefficient, λ is the wavelength of the optical beam and L is the propagation distance. The attenuation coefficient $\mathcal{C}(\lambda)$ is the sum of absorption and scattering coefficients $\varrho_a(\lambda)$ and $\varrho_s(\lambda)$, respectively. The dependency of both absorption and scattering coefficients on the wavelength of the optical beam was presented empirically for pure water in [31]. Then, a model was built mainly using the chlorophyll concentration together with several constituents in the underwater medium expressing the absorption and scattering coefficients as [32]

$$\varrho_a(\lambda) = \varrho_{a,w}(\lambda) + \varrho_{a,cl}(\lambda) + \varrho_{a,f}(\lambda) + \varrho_{a,h}(\lambda), \quad (2)$$

$$\varrho_b(\lambda) = \varrho_{b,w}(\lambda) + \varrho^0_{b,s}(\lambda)C_s + \varrho^0_{b,l}(\lambda)C_l, \quad (3)$$

where $\varrho_{a,w}(\lambda)$ is the absorption coefficient of pure water [31], $\varrho_{a,cl} = \varrho^0_{a,c}(\lambda)\left(\frac{C_c}{C^0_c}\right)^{0.602}$ is the absorption coefficient of the chlorophyll, $\varrho^0_{a,c}(\lambda)$ is the specific absorption coefficient of the chlorophyll, C_c shows the total chlorophyll concentration in mg/m^3, $C^0_c = 1\,\text{mg/m}^3$ denotes the chlorophyll concentration, $\varrho_{a,f}(\lambda) = \varrho^0_{a,f}C_f\exp(-k_f\lambda)$ and $\varrho^0_{a,f} = 35.959\,\text{m}^2/\text{mg}$ are respectively the absorption coefficient and the specific absorption of the fulvic acid, $C_f = 1.74098C_ce^{\frac{0.12327C_c}{C^0_c}}$ in mg/m^3 is the concentration of fulvic acid, $k_f = \frac{0.0189}{\text{nm}}$, $\varrho_{a,h}(\lambda) = \varrho^0_{a,h}C_h\exp(-k_h\lambda)$ indicates the absorption coefficient of humic acid, $\varrho^0_{a,h} = 18.828\,\text{m}^2/\text{mg}$ and $C_h = 0.19334C_ce^{\frac{0.12343C_c}{C^0_c}}$ in mg/m^3 are respectively the specific absorption and the concentration of humic acid, and $k_h = \frac{0.01105}{\text{nm}}$. For scattering coefficient $\varrho_b(\lambda)$, we have $\varrho_{b,w}(\lambda) = 0.005826\left(\frac{400}{\lambda}\right)^{4.322}$ as the scattering coefficient of pure water [31], $\varrho^0_{b,s}(\lambda) = 1.151302\left(\frac{400}{\lambda}\right)^{1.7}$ and $\varrho^0_{b,l}(\lambda) = 0.3411\left(\frac{400}{\lambda}\right)^{0.3}$ are the scattering by small and large particles, respectively, $C_s = 0.01739C_ce^{\frac{0.11631C_c}{C^0_c}}$ and $C_l = 0.76284C_ce^{\frac{0.03092C_c}{C^0_c}}$. While the attenuation described by the Beer-Lambert Law does not consider the effects of multiple sources of attenuation such as practical scattering and beam spreading, it provides an adequate model for weak scattering [31] which matches the empirical turbulence model of a clean ocean environment as explained in the following section.

2) Underwater Turbulence: In a recently introduced WGG model, the statistics of laser beam irradiance fluctuations is characterized by mixing the Weibull and GG distributions and its accuracy has been verified through the experimental measurements [30]. The experiment emulated a realistic clean ocean underwater environment to investigate the effects of thermohaline gradient, salinity gradient and air bubbles on turbulence strength. The results indicated that the statistical model of the irradiance fluctuations has a double-peaked distribution, particularly induced by the effect of air bubbles. Compared with EGG, the study showed that a combined Weibull-GG distribution offered an excellent goodness of fit for moderate and strong turbulence regimes. The PDF of the WGG distribution model is expressed as [30]:

$$f_{h_{at}}(h_{at}) = \frac{\omega k}{\varpi^k}h_{at}^{k-1}\exp\left(-\frac{h_{at}^k}{\varpi^k}\right) + \frac{(1-\omega)c}{b^{ac}\Gamma(a)}h_{at}^{ac-1}\exp\left(-\frac{h_{at}^c}{b^c}\right), \quad (4)$$

where $h_{at} > 0$, ω is the mixing ratio for Weibull and GG distributions, ϖ and k are the scale and shape parameters for Weibull distribution, b is the scale parameter of GG distribution, while a and c are the shape parameters of GG distribution. The details of parameters for mixed Weibull and GG distribution are given in [30] and [33] which depend on the temperature and salinity gradients and the air bubbles in the underwater medium.

3) Pointing Error: In UOWC systems, pointing errors arise due to beam misalignment caused by platform instability, Tx/Rx motion, and turbulence-induced fluctuations. Accurate statistical modeling of these errors remains essential for evaluating system performance. The Hoyt distribution is well-suited for modeling asymmetric beam misalignment in UOWC systems. Unlike symmetric models such as the Rayleigh distribution, which assume equal variance in all directions, the Hoyt distribution accounts for the asymmetric beam misalignment where the horizontal and vertical beam misalignments exhibit different variances. Mathematically, if the beam centroid displacement in the horizontal and vertical directions follows two independent Gaussian distributions with different standard deviations (*i.e.*, σ_z and σ_s), then the joint angular and radial displacement φ and r_d of the beam follow a Hoyt distribution given by [34]:

$$f_{r_d,\varphi}(r_d,\varphi) = \frac{r_d}{2\pi q_H\sigma_s^2}e^{-\frac{r_d^2\xi(\varphi)}{2\sigma_s^2}}, \quad (5)$$

where $\xi(\varphi) = \left[1-(1-q_H^2)\cos^2\varphi\right]/q_H^2$, and $q_H = \sigma_z/\sigma_s, \in (0,1]$. In [34], the pointing error was expressed in integral form as

$$f_{pl}(h_{pl}) = \frac{\eta_s^2}{2\pi q_H}\int_{-\pi}^{\pi}\frac{h_{pl}^{\eta_s^2\xi(\varphi)-1}}{A_0^{\eta_s^2\xi(\varphi)}}\mathrm{d}\varphi, \quad (6)$$

where $\eta_s = \omega_e/(2\sigma_s)$, $\omega_e = \omega_b[\sqrt{\pi}\text{erf}(\upsilon)/(2\upsilon e^{-\upsilon^2})]^{\frac{1}{2}}$, ω_b is the beamwaist, erf$(\cdot)$ is the error function, $\upsilon = \frac{(\pi r_a^2/2)^{0.5}}{\omega_b}$, $r_a = D_G/2$ is the Rx aperture radius, D_G is the Rx aperture diameter, and $A_0 = \text{erf}^2(\upsilon)$.

4) AOA Fluctuations: AOA fluctuations significantly impact the received signal quality by introducing random variations in the alignment between the transmitted and received optical beams. The Rayleigh distribution model provides an analytically tractable way to characterize the impact of AOA variations on system performance metrics such as BER, OP and SNR. According to the Rayleigh distribution, the PDF of the random variable θ_d that illustrates the angular deviation can be stated by [35]:

$$f_{\theta_d}(\theta_d) = \frac{\theta_d}{\sigma_0^2}\exp\left(-\frac{\theta_d^2}{2\sigma_0^2}\right), \quad (7)$$

where σ_0^2 stands for the variance of θ_d.

C. Signal Model

Assuming that a ORIS module includes $\mathcal{N} = \mathcal{N}_1 + \mathcal{N}_2$ number of elements where $\mathcal{N}_1$ passive and $\mathcal{N}_2$ active ORIS elements are allocated for IT and EH, respectively. Then, the received information signal can be written as:

$$y = \sum_{n=1}^{\mathcal{N}_1} h_n g_n \beta_{r,n} e^{j\theta_n} + \sum_{i=1}^{\mathcal{N}_2} h_i g_i \rho_i e^{j\theta_i} + \sum_{i=1}^{\mathcal{N}_2} n_{t,i} + n_0, \quad (8)$$

where $h_n = v_n e^{-j\phi_n}$ and $g_n = u_n e^{-j\varphi_n}$ are the channel gains for source-ORIS and ORIS-user links, $\beta_{r,n} \in (0, 1]$ is the reflection coefficient of each passive ORIS element, $\theta_n \in (0, 2\pi)$ is the phase shift introduced by ORIS element, x is the transmitted signal, the term $\sum_{i=1}^{\mathcal{N}_2} h_i g_i \rho_i e^{j\theta_i}$ denotes the signal interference on the received information signal arising from active ORIS elements, $h_i = v_i e^{-j\phi_i}$, $g_i = u_i e^{-j\varphi_i}$, ρ_i is the amplification factor for each active ORIS element, $n_{t,i} \sim (0, \sigma_{t,i}^2)$ is the thermal noise for each active ORIS elements with variance $\sigma_{t,i}^2$, $n_0 \sim (0, \sigma_n^2)$ is the additive white Gaussian noise (AWGN) with variance σ_n^2.

The channel gains are represented in their complex baseband equivalent form, where the magnitude captures fading amplitude while the phase accounts for propagation delay and reflection geometry. This representation is adopted to model the controllable phase adjustment introduced by the ORIS elements. Assuming that all passive and active ORIS elements are identical within themselves *i.e.*, $\beta_{r,n} = \beta$, $\rho_i = \rho$ and $n_t \sim (0, \sigma_t^2)$, and maximum signal-to-interference-plus-noise-ratio (SINR) is provided *i.e.*, $\phi_n + \varphi_n = \theta_n$, where the phase shift introduced by RIS is assumed to be compensated, then the instantaneous SINR for heterodyne detection is given by

$$\gamma = \frac{P_t \left(\sum_{n=1}^{\mathcal{N}_1} v_n u_n \beta \right)}{P_t \left(\sum_{i=1}^{\mathcal{N}_2} v_i u_i \rho \right) + \mathcal{N}_2 \sigma_t^2 + \sigma_n^2}, \quad (9)$$

where P_t is the transmitted power. The inclusion of active ORIS interference in the denominator introduces a coupling between system parameters that makes analytical derivations highly complex and intractable. To simplify the model and enable tractable analysis, we approximate the cumulative interference from active RISs as a random variable characterized by its statistical variance with $(0, \sigma_i^2)$. Then, the instantaneous SINR for independent and identically distributed (i.i.d) fading channel for heterodyne detection becomes $\gamma = \mathcal{N}_1 \beta \mathcal{H} \overline{\gamma}$, given that $\mathcal{H} = v_n u_n$, $\overline{\gamma} = P_t/\sigma_p^2$ and $\sigma_p^2 = \mathcal{N}_2(\sigma_i^2 + \sigma_t^2) + \sigma_n^2$.

For IM/DD scheme, the instantaneous SINR can be expressed by

$$\gamma = \frac{P_t \left(\sum_{n=1}^{\mathcal{N}_1} v_n u_n \beta \right)^2}{P_t \left(\sum_{i=1}^{\mathcal{N}_2} v_i u_i \rho \right) + \mathcal{N}_2 \sigma_t^2 + \sigma_n^2}. \quad (10)$$

Using the assumption given for Eqs. (9) and the i.i.d. fading channel for IM/DD detection, the instantaneous SINR can be obtained by

$$\gamma = (\mathcal{N}_1 \beta \mathcal{H})^2 \overline{\gamma}, \quad (11)$$

where $\overline{\gamma} = P_t^2/\sigma_p^2$. It follows that the expression of instantaneous SINR heterodyne and IM/DD detection schemes can be written jointly as:

$$\gamma = (\mathcal{N}_1 \beta \mathcal{H})^r \overline{\gamma}, \quad (12)$$

where $r = 1$ and $r = 2$ denote the heterodyne and IM/DD detection schemes, respectively.

III. Probabilistic Analysis

This section provides the probabilistic analysis of fading channel by taking into account the combined effect of underwater turbulence, attenuation, pointing error and AOA fluctuations. Then, the unified PDF of the SNR is obtained for both heterodyne and IM/DD schemes.

The channel state in Eq. (1) combines the effects of attenuation h_{al}, turbulence h_{at}, pointing error h_{pe} and AOA fluctuations h_{af}. While h_{al} is deterministic, the others vary randomly and remain as random variables (RVs). To step further, we define $h_{ag} = h_{al} h_{at} h_{pe}$ and the condition h_{pe} over orientation deviation θ_d that results in the conditioned PDF as

$$f_{h_{ag}|\theta_d}(h_{ag}) = \int_{\Delta_1}^{\infty} \frac{f_{h_{at}}(h_{at})}{h_{al} h_{at}} f_{h_{pe}|\theta_d} \left(\frac{h_{ag}}{h_{al} h_{at}} \right) \mathrm{d}h_{at}, \quad (13)$$

where $\Delta_1 = \frac{h_{ag}}{h_{al} A_0 \cos\theta_d}$. Following the steps given in APPENDIX-A, the conditioned PDF $f_{h_{ag}|\theta_d}(h_{ag})$ can be found as given in Eq. (A.3).

A. Channel PDF

The PDF of the channel can be calculated by using

$$f_{\mathcal{H}}(\mathcal{H}) = \int_0^{\theta_{FOV}} f_{h_{ag}|\theta_d}(\mathcal{H}) f_{\theta_d}(\theta_d) \mathrm{d}\theta_d + \delta(\mathcal{H}) \int_{\theta_{FOV}}^{\infty} f_{\theta_d}(\theta_d) \mathrm{d}\theta_d, \quad (14)$$

where θ_{FOV} is the field-of-view (FoV) and $\delta(\cdot)$ is the impulse function. Following the derivation given in APPENDIX-B, the PDF of the channel state is found to be

$$f_{\mathcal{H}}(\mathcal{H}) = \delta(\mathcal{H}) \Delta_2 + \frac{\omega \eta_s^2 \Delta_3}{2\pi q_H} \int_{-\pi}^{\pi} \frac{\mathcal{H}^{\eta_s^2 \xi(\varphi) - 1}}{(A_0 h_{al} \varpi)^{\eta_s^2 \xi(\varphi)}} \times \Gamma\left(\frac{k - \eta_s^2 \xi(\varphi)}{k}, \left(\frac{\Delta_4}{\varpi} \right)^k \right) \mathrm{d}\varphi + \frac{(1-\omega)\eta_s^2 \Delta_3}{2\pi q_H \Gamma(a)} \times \int_{-\pi}^{\pi} \frac{\mathcal{H}^{\eta_s^2 \xi(\varphi) - 1}}{(A_0 h_{al} b)^{\eta_s^2 \xi(\varphi)}} \Gamma\left(\frac{ac - \eta_s^2 \xi(\varphi)}{c}, \left(\frac{\Delta_4}{b} \right)^c \right) \mathrm{d}\varphi, \quad (15)$$

where $\Delta_2 = \exp\left(-\frac{\theta_{FOV}^2}{2\sigma_0^2} \right)$, $\Delta_3 = 1 - \Delta_2$, $\Delta_4 = \mathcal{H}/(A_0 h_{al})$ and $\Gamma(a, b)$ is the upper incomplete gamma function.

B. Unified PDF of the SNR

Using the PDF transform formula to find the unified PDF of the instantaneous SINR together with Eq. (11), the PDF of the SINR can be found by

$$f_\gamma(\gamma) = f_{\mathcal{H}}\left(\frac{(\gamma/\overline{\gamma})^{\frac{1}{r}}}{\mathcal{N}_1\beta}\right)\left|\frac{\mathrm{d}\mathcal{H}}{\mathrm{d}\gamma}\right| = \frac{\gamma^{\frac{1}{r}-1}}{r\overline{\gamma}^{\frac{1}{r}}\mathcal{N}_1\beta} f_{\mathcal{H}}\left(\frac{(\gamma/\overline{\gamma})^{\frac{1}{r}}}{\mathcal{N}_1\beta}\right). \tag{16}$$

Now, inserting Eq. (15) into Eq. (16), then utilizing [36, Eq. (06.06.26.0005.01)] to express upper incomplete gamma function depending on the Meijer's G function and using [36, Eq. (07.34.17.0011.01)] to simplify the Meijer's G function, respectively, the unified PDF of the SINR is given by:

$$\begin{aligned} f_\gamma(\gamma) = {} & \frac{\omega\eta_s^2\Delta_3}{2\pi q_H r}\int_{-\pi}^{\pi}\frac{1}{\gamma}G_{1,2}^{2,0}\left(\frac{(\gamma/\overline{\gamma})^{\frac{k}{r}}}{(\varpi\Delta_5)^k}\middle|\begin{matrix}\frac{k+\eta_s^2\xi(\varphi)}{k}\\ \frac{\eta_s^2\xi(\varphi)}{k},1\end{matrix}\right)\mathrm{d}\varphi \\ & + \frac{(1-\omega)\eta_s^2\Delta_3}{2\pi q_H\Gamma(a) r}\int_{-\pi}^{\pi}\frac{1}{\gamma}G_{1,2}^{2,0}\left(\frac{(\gamma/\overline{\gamma})^{\frac{c}{r}}}{(b\Delta_5)^c}\middle|\begin{matrix}\frac{c+\eta_s^2\xi(\varphi)}{c}\\ \frac{\eta_s^2\xi(\varphi)}{c},a\end{matrix}\right)\mathrm{d}\varphi \\ & + \frac{\gamma^{\frac{1}{r}-1}}{r\overline{\gamma}^{\frac{1}{r}}\mathcal{N}_1\beta}\Delta_2\delta\left(\frac{\gamma^{\frac{1}{r}}}{\overline{\gamma}^{\frac{1}{r}}\mathcal{N}_1\beta}\right), \end{aligned} \tag{17}$$

where $\Delta_5 = A_0 h_{al}\mathcal{N}_1\beta$, and $G_{p,q}^{m,n}\left(x\middle|\begin{matrix}a_i\\ b_i\end{matrix}\right)$ is the Meijer's G function.

C. Cumulative Distribution Function (CDF) of the SNR

The CDF of the SNR can be found by using $F_\gamma(\gamma) = \int_0^\gamma f_\gamma(x)\mathrm{d}x$. Following the derivation steps given in APPENDIX-C, the CDF of the SNR is found to be

$$\begin{aligned} F_\gamma(\gamma) = {} & \frac{\omega\eta_s^2\Delta_3}{2\pi q_H k}\int_{-\pi}^{\pi}G_{2,3}^{2,1}\left(\frac{(\gamma/\overline{\gamma})^{\frac{k}{r}}}{(\varpi\Delta_5)^k}\middle|\begin{matrix}1,\frac{k+\eta_s^2\xi(\varphi)}{k}\\ \frac{\eta_s^2\xi(\varphi)}{k},1,0\end{matrix}\right)\mathrm{d}\varphi \\ & + \frac{(1-\omega)\eta_s^2\Delta_3}{2\pi q_H\Gamma(a)c}\int_{-\pi}^{\pi}G_{2,3}^{2,1}\left(\frac{(\gamma/\overline{\gamma})^{\frac{c}{r}}}{(b\Delta_5)^c}\middle|\begin{matrix}1,\frac{c+\eta_s^2\xi(\varphi)}{c}\\ \frac{\eta_s^2\xi(\varphi)}{c},a,0\end{matrix}\right)\mathrm{d}\varphi \\ & + \Delta_2 H\left(\frac{\gamma^{\frac{1}{r}}}{\overline{\gamma}^{\frac{1}{r}}\mathcal{N}_1\beta}\right), \end{aligned} \tag{18}$$

where $H(\cdot)$ is the Heaviside function.

IV. Exact Analysis of Performance Metrics

A. OP Analysis

The OP is defined as the probability of instantaneous SNR γ falls below the defined threshold channel level γ_{th} *i.e.*, $P_{out} = P(\gamma \le \gamma_{th}) = F_\gamma(\gamma_{th})$. Inserting the CDF given in Eq. (18), the OP can be expressed as:

$$\begin{aligned} P_{out} = {} & \frac{\omega\eta_s^2\Delta_3}{2\pi q_H k}\int_{-\pi}^{\pi}G_{2,3}^{2,1}\left(\frac{(\gamma_{th}/\overline{\gamma})^{\frac{k}{r}}}{(\varpi\Delta_5)^k}\middle|\begin{matrix}1,\frac{k+\eta_s^2\xi(\varphi)}{k}\\ \frac{\eta_s^2\xi(\varphi)}{k},1,0\end{matrix}\right)\mathrm{d}\varphi \\ & + \frac{(1-\omega)\eta_s^2\Delta_3}{2\pi q_H\Gamma(a)c}\int_{-\pi}^{\pi}G_{2,3}^{2,1}\left(\frac{(\gamma_{th}/\overline{\gamma})^{\frac{c}{r}}}{(b\Delta_5)^c}\middle|\begin{matrix}1,\frac{c+\eta_s^2\xi(\varphi)}{c}\\ \frac{\eta_s^2\xi(\varphi)}{c},a,0\end{matrix}\right)\mathrm{d}\varphi \\ & + \Delta_2 H\left(\frac{\gamma_{th}^{\frac{1}{r}}}{\overline{\gamma}^{\frac{1}{r}}\mathcal{N}_1\beta}\right). \end{aligned} \tag{19}$$

B. Average BER Analysis

A unified expression for the average BER that encompasses various modulation schemes can be formulated as [37]

$$P_e = \frac{\delta}{2\Gamma(p)}\sum_{s=1}^{n_x}\int_0^\infty \Gamma(p, q_s\gamma) f_\gamma(\gamma)\mathrm{d}\gamma, \tag{20}$$

where all related parameters for different types of detection and modulation schemes are listed in [38]. Finally, applying the procedures given in APPENDIX-D, the average BER can be expressed by Eq. (22), as shown at the bottom of the next page, where $H_{p,q}^{m,n}\left(x\middle|\begin{matrix}(a_i,\alpha_i)\\ (b_j\beta_j)\end{matrix}\right)$ is the Fox-H function.

C. Ergodic Capacity Analysis

The ergodic capacity can be expressed as [39]:

$$\overline{C} \triangleq \mathbb{E}\left[\log_2\left(1+c_r\gamma\right)\right] = \int_0^\infty \frac{\ln(1+c_r\gamma)}{\ln(2)} f_\gamma(\gamma)d\gamma, \tag{21}$$

where c_r is the constant having the values of $c_1 = 1$ and $c_2 = e/(2\pi)$ for heterodyne (*i.e.* $r = 1$) and IM/DD (*i.e.* $r = 2$) schemes, respectively. Finally, using the derivations given in APPENDIX-E, the ergodic channel capacity is found to be as in Eq. (31), as shown at the bottom of the next page.

V. High SINR Asymptotic Analysis

Due to the challenging nature of underwater medium, it is important to provide the behavior of the channel for a wide range of SINR values, to observe the optimal performance level. For this reason, in this section we consider the performance analysis for high-SINR, and their approximations are presented.

A. OP

Using Eq. (F.1) to convert two Meijer-G functions in Eq. (19) and then applying Eqs. (F.2) and (F.3), the OP can be approximated in high SNR regimes as below:

$$\begin{aligned} P_{out} = {} & \frac{\omega\eta_s^2\Delta_3}{2\pi q_H}\int_{-\pi}^{\pi}\left(\sum_{j=1}^{2}\frac{\Psi_{aj}}{\overline{\gamma}^{\theta_{aj}}}\right)\mathrm{d}\varphi + \frac{(1-\omega)}{2\pi q_H} \\ & \times \frac{\eta_s^2\Delta_3}{\Gamma(a)}\int_{-\pi}^{\pi}\left(\sum_{j=1}^{2}\frac{\Psi_{bj}}{\overline{\gamma}^{\theta_{bj}}}\right)\mathrm{d}\varphi + \Delta_2 H\left(\frac{(\gamma_{th}/\overline{\gamma})^{\frac{1}{r}}}{\mathcal{N}_1\beta}\right), \end{aligned} \tag{23}$$

where

$$\begin{aligned} \Psi_{a1} &= \frac{1}{\eta_s^2\xi(\varphi)}\Gamma\left(\frac{k-\eta_s^2\xi(\varphi)}{k}\right)\left[\frac{\gamma_{th}}{(\varpi\Delta_5)^r}\right]^{\frac{\eta_s^2\xi(\varphi)}{r}} \\ \Psi_{a2} &= \frac{1}{\Gamma(2)\left(\eta_s^2\xi(\varphi)-k\right)}\left[\frac{\gamma_{th}}{(\varpi\Delta_5)^r}\right]^{\frac{k}{r}}, \\ \Psi_{b1} &= \frac{1}{\eta_s^2\xi(\varphi)}\Gamma\left(\frac{ac-\eta_s^2\xi(\varphi)}{c}\right)\left[\frac{\gamma_{th}}{(b\Delta_5)^r}\right]^{\frac{\eta_s^2\xi(\varphi)}{r}} \\ \Psi_{b2} &= \frac{1}{a\left(\eta_s^2\xi(\varphi)-ac\right)}\left[\frac{\gamma_{th}}{(b\Delta_5)^r}\right]^{\frac{ac}{r}}, \end{aligned} \tag{24, 25}$$

$$\theta_{a1}=\theta_{b1}=\frac{\eta_s^2\xi(\varphi)}{r},\qquad \theta_{a2}=\frac{k}{r},\theta_{b2}=\frac{ac}{r}. \tag{26}$$

B. Average BER

By employing Eqs. (F.2) and (F.3), the high SNR regime approximation for average BER can be found by

$$P_e=\frac{\delta\omega\eta_s^2\Delta_3}{4\pi q_H\Gamma(p)}\sum_{s=1}^{n_x}\int_{-\pi}^{\pi}\left(\sum_{j=1}^{2}\frac{\Upsilon_{cj}}{\overline{\gamma}^{\theta_{cj}}}\right)\mathrm{d}\varphi + \frac{\delta(1-\omega)\eta_s^2\Delta_3}{4\pi q_H\Gamma(p)\Gamma(a)}\sum_{s=1}^{n_x}\int_{-\pi}^{\pi}\left(\sum_{j=1}^{2}\frac{\Upsilon_{dj}}{\overline{\gamma}^{\theta_{dj}}}\right)\mathrm{d}\varphi+\frac{n_x\delta}{2}\Delta_2, \tag{27}$$

where

$$\Upsilon_{c1}=\frac{\left(\varpi\Delta_5 q_s^{\frac{1}{r}}\right)^{-\eta_s^2\xi(\varphi)}}{\eta_s^2\xi(\varphi)}\Gamma\left(\frac{k-\eta_s^2\xi(\varphi)}{k}\right)\Gamma\left(p+\frac{\eta_s^2\xi(\varphi)}{r}\right)$$

$$\Upsilon_{c2}=\frac{1}{(\eta_s^2\xi(\varphi)-k)}\Gamma\left(p+\frac{k}{r}\right)\left(\frac{1}{\varpi\Delta_5 q_s^{\frac{1}{r}}}\right)^{k}, \tag{28}$$

$$\Upsilon_{d1}=\frac{\left(b\Delta_5 q_s^{\frac{1}{r}}\right)^{-\eta_s^2\xi(\varphi)}}{\eta_s^2\xi(\varphi)}\Gamma\left(\frac{ac-\eta_s^2\xi(\varphi)}{c}\right)\Gamma\left(p+\frac{\eta_s^2\xi(\varphi)}{r}\right)$$

$$\Upsilon_{d2}=\frac{1}{a\left(\eta_s^2\xi(\varphi)-ac\right)}\Gamma\left(p+\frac{ac}{r}\right)\left(\frac{1}{b\Delta_5 q_s^{\frac{1}{r}}}\right)^{ac}, \tag{29}$$

$$\theta_{c1}=\theta_{d1}=\frac{\eta_s^2\xi(\varphi)}{r},\qquad \theta_{c2}=\frac{k}{r},\theta_{d2}=\frac{ac}{r}. \tag{30}$$

VI. Joint OP Analysis for SWIPT

Using $\mathcal{N}_1$ and $\mathcal{N}_2$ ORIS elements for IT and EH, the joint OP for energy-data rate can be expressed by

$$P_{\mathcal{J}}=\Pr\left[Q_{ii}\le E_{ii}\cup R_{ii}\le\log_2(1+\gamma)\right], \tag{32}$$

where index $ii\in\{ES,PS,TS\}$ for ES, PS and TS approaches, Q is the harvested energy, E is the required energy, R is the instantaneous data rate. The ES, PS and TS approaches for SWIPT application will be analyzed in the next subsections.

A. Element Splitting

The received power signal can be written as:

$$y=\eta P_t^{\frac{r}{2}}\sum_{i=1}^{\mathcal{N}_2}h_i g_i\rho_i e^{j\theta_i}+\sum_{i=1}^{\mathcal{N}_2}n_{t,i}+n_0, \tag{33}$$

where η is the photodetector efficiency. Using channel parameters given in Section-II-C, it is possible to write the harvested energy as

$$Q_{ES}=\eta^2 P_t^r\rho^2\left(\sum_{i=1}^{\mathcal{N}_2}\mathcal{H}\right)^2, \tag{34}$$

while the required energy in Eq. (32) can be expressed as $E_{ES}=P_{RIS}^{ACT}+\mathcal{N}_2(\rho P_e+P_{DC})+P_{rx}$, where P_{RIS}^{ACT} is the power of amplified signal reflected by the active ORIS elements, P_e is the power consumption of each active element, P_{DC} is the direct current biasing power used by the amplifier in each active ORIS element, and P_{rx} is the power level requested by the Rx, [40]. Also, using SNR definition in Eq. (12), the instantaneous data rate is given by:

$$R_{ES}=\log_2\left[1+(\mathcal{N}_1\beta\mathcal{H})^r\overline{\gamma}\right]. \tag{35}$$

Using the expression given in Eq. (32), the joint OP for ES approach can be written as $P_{\mathcal{J}}^{ES}=P_{\mathcal{J}_1}^{ES}+P_{\mathcal{J}_2}^{ES}-P_{\mathcal{J}_1}^{ES}P_{\mathcal{J}_2}^{ES}$, where $P_{\mathcal{J}_1}^{ES}$ and $P_{\mathcal{J}_2}^{ES}$ are

$$P_{\mathcal{J}_1}^{ES}=P_r\left(\mathcal{H}\le\frac{\sqrt{E_{ES}}}{\eta\mathcal{N}_2\rho P_t^{\frac{r}{2}}}\right),\quad P_{\mathcal{J}_2}^{ES}=P_r\left(\mathcal{H}\le\frac{\gamma_{th}^{\frac{1}{r}}}{\mathcal{N}_1\beta\overline{\gamma}^{\frac{1}{r}}}\right), \tag{36}$$

which can be both calculated by using Eq. (G.2) given in APPENDIX-G based on the equality $P_r(\mathcal{H}<\mathcal{Z})=F_{\mathcal{H}}(\mathcal{Z})$.

B. Power Splitting

Assuming $\mathcal{N}_1=\mathcal{N}_2=\mathcal{N}$ are all passive ORIS elements, and ζ is the portion of power dedicated to power transfer, the received information and power signals are respectively

$$y_I=(1-\zeta)\sum_{n=1}^{\mathcal{N}}h_n g_n\beta_n e^{j\theta_n}+\zeta\sum_{i=1}^{\mathcal{N}}h_i g_i\beta_i e^{j\theta_i}+n_0, \tag{37}$$

$$P_e=\frac{\delta\omega\eta_s^2\Delta_3}{4\pi q_H r\Gamma(p)}\sum_{s=1}^{n_x}\int_{-\pi}^{\pi}H_{3,3}^{2,2}\left(\frac{1}{(\varpi\Delta_5)^k(q_s\overline{\gamma})^{\frac{k}{r}}}\middle|\begin{matrix}\left(1,\frac{k}{r}\right),\left(1-p,\frac{k}{r}\right),\left(\frac{k+\eta_s^2\xi(\varphi)}{k},1\right)\\ \left(\frac{\eta_s^2\xi(\varphi)}{k},1\right),(1,1),\left(0,\frac{k}{r}\right)\end{matrix}\right)\mathrm{d}\varphi + \frac{\delta(1-\omega)\eta_s^2\Delta_3}{4\pi q_H r\Gamma(p)\Gamma(a)}\sum_{s=1}^{n_x}\int_{-\pi}^{\pi}H_{3,3}^{2,2}\left(\frac{1}{(b\Delta_5)^c(q_s\overline{\gamma})^{\frac{c}{r}}}\middle|\begin{matrix}\left(1,\frac{c}{r}\right),\left(1-p,\frac{c}{r}\right),\left(\frac{c+\eta_s^2\xi(\varphi)}{c},1\right)\\ \left(\frac{\eta_s^2\xi(\varphi)}{c},1\right),(a,1),\left(0,\frac{c}{r}\right)\end{matrix}\right)\mathrm{d}\varphi+\frac{n_x\delta}{2}\Delta_2, \tag{22}$$

$$\overline{C}=\frac{\omega\eta_s^2\Delta_3}{2\pi q_H r\ln(2)}\int_{-\pi}^{\pi}H_{3,4}^{4,1}\left(\frac{1}{(\varpi\Delta_5)^k(c_r\overline{\gamma})^{\frac{k}{r}}}\middle|\begin{matrix}\left(0,\frac{k}{r}\right),\left(1,\frac{k}{r}\right),\left(\frac{k+\eta_s^2\xi(\varphi)}{k},1\right)\\ \left(\frac{\eta_s^2\xi(\varphi)}{k},1\right),(1,1),\left(0,\frac{k}{r}\right),\left(0,\frac{k}{r}\right)\end{matrix}\right)\mathrm{d}\varphi + \frac{(1-\omega)\eta_s^2\Delta_3}{2\pi q_H r\Gamma(a)\ln(2)}\int_{-\pi}^{\pi}H_{3,4}^{4,1}\left(\frac{1}{(b\Delta_5)^c(c_r\overline{\gamma})^{\frac{c}{r}}}\middle|\begin{matrix}\left(0,\frac{c}{r}\right),\left(1,\frac{c}{r}\right),\left(\frac{c+\eta_s^2\xi(\varphi)}{c},1\right)\\ \left(\frac{\eta_s^2\xi(\varphi)}{c},1\right),(a,1),\left(0,\frac{c}{r}\right),\left(0,\frac{c}{r}\right)\end{matrix}\right)\mathrm{d}\varphi. \tag{31}$$

and

$$y_P = \eta(\zeta P_t)^{\frac{r}{2}} \sum_{i=1}^{\mathcal{N}} h_i g_i \beta_i e^{j\theta_i} + n_0. \tag{38}$$

We can express the instantaneous data rate and harvested energy respectively as

$$R_{PS} = \log_2\left[1 + ((1-\zeta)\mathcal{N}\beta\mathcal{H})^r \overline{\gamma}\right], \tag{39}$$

and

$$Q_{PS} = \eta^2 \zeta^r P_t^r \beta^2 \left(\sum_{i=1}^{\mathcal{N}} \mathcal{H}\right)^2, \tag{40}$$

while the required energy in Eq. (32) is $E_{PS} = \mathcal{N}P_e + P_c$, [40]. Then, using the expression given in Eq. (32), the joint OP for PS takes the form of $P_{\mathcal{J}}^{PS} = P_{\mathcal{J}_1}^{PS} + P_{\mathcal{J}_2}^{PS} - P_{\mathcal{J}_1}^{PS} P_{\mathcal{J}_2}^{PS}$, where $P_{\mathcal{J}_1}^{PS}$ and $P_{\mathcal{J}_2}^{PS}$ are respectively $P_{\mathcal{J}_1}^{PS} = P_r\left(\mathcal{H} \le \frac{\sqrt{E_{PS}}}{\eta\mathcal{N}\beta(\zeta P_t)^{\frac{r}{2}}}\right)$, and $P_{\mathcal{J}_2}^{PS} = P_r\left(\mathcal{H} \le \frac{(\gamma_{th}/\overline{\gamma})^{\frac{1}{r}}}{(1-\zeta)\mathcal{N}\beta}\right)$, which can be calculated by using Eq. (G.2) given in APPENDIX-G according to equality $P_r(\mathcal{H} < \mathcal{Z}) = F_{\mathcal{H}}(\mathcal{Z})$.

C. Time Switching

Assuming that the symbol time duration T is divided into two parts and first τ time interval is used for energy harvesting, the received information and power signals can be respectively written as

$$y_I = \sum_{n=1}^{\mathcal{N}} h_n g_n \beta_n e^{j\theta_n} + \sum_{i=1}^{\mathcal{N}} h_i g_i \beta_i e^{j\theta_i} + n_0, \tag{41}$$

and

$$y_P = \eta P_t^{\frac{r}{2}} \sum_{i=1}^{\mathcal{N}} h_i g_i \beta_i e^{j\theta_i} + n_0. \tag{42}$$

Then, the instantaneous data rate R_{TS} and harvested energy Q_{TS} will be respectively

$$R_{TS} = (1-\tau)\log_2\left[1 + (\mathcal{N}\beta\mathcal{H})^r \overline{\gamma}\right], \tag{43}$$

and

$$Q_{TS} = \tau\eta^2 P_t^r \beta^2 \left(\sum_{i=1}^{\mathcal{N}} \mathcal{H}\right)^2, \tag{44}$$

while the required energy in Eq. (32) can be written as $E_{TS} = (1-\tau)\mathcal{N}P_e + P_c$, [40]. It follows that, according to the expression given in Eq. (32), the joint OP for TS is found to be $P_{\mathcal{J}}^{TS} = P_{\mathcal{J}_1}^{TS} + P_{\mathcal{J}_2}^{TS} - P_{\mathcal{J}_1}^{TS} P_{\mathcal{J}_2}^{TS}$, where $P_{\mathcal{J}_1}^{TS}$ and $P_{\mathcal{J}_2}^{TS}$ are respectively $P_{\mathcal{J}_1}^{TS} = P_r\left(\mathcal{H} \le \frac{\sqrt{E_{PS}}}{\sqrt{\tau}\eta\mathcal{N}\beta P_t^{\frac{r}{2}}}\right)$, and $P_{\mathcal{J}_2}^{TS} = P_r\left(\mathcal{H} \le \frac{\left[(1+\gamma_{th})^{\frac{1}{1-\tau}} - 1\right]^{\frac{1}{r}}}{\mathcal{N}\beta\overline{\gamma}^{\frac{1}{r}}}\right)$, which can be calculated by using Eq. (G.2) given in APPENDIX-G according to the equality $P_r(\mathcal{H} < \mathcal{Z}) = F_{\mathcal{H}}(\mathcal{Z})$.

Algorithm 1 describes the main steps of the pseudocode for the computation of the joint OP in case of different SWIPT protocols. We notice that the computational cost of this pseudocode is $\mathcal{O}(\mathcal{N})$. Indeed, all the derived closed-form expressions for the OPs are evaluated through Meijer-G functions, whose computation scales linearly with the number of RIS elements, providing a significantly lower burden than iterative optimization algorithms commonly used in RIS literature. Furthermore, unlike iterative optimization-based RIS or SWIPT schemes (*e.g.*, [41], [42]), which rely on repeated numerical searches for phase-shift and power-allocation parameters, the proposed framework derives closed-form expressions under realistic underwater conditions. This analytical approach eliminates convergence uncertainty and provides direct physical insight, while maintaining comparable accuracy with significantly lower computational cost or higher for iterative algorithms [43].

Algorithm 1 Pseudocode for the Computation of the Joint OP for ORIS-Assisted SWIPT-UOWC System

Require: ProtocolType $\in$ {ES, PS, TS},
SystemParameters: $\mathcal{N}$, $\mathcal{N}_1$, $\mathcal{N}_2$, β, ρ, ζ, τ, P_t,η, P_{rx}, γ_{th}
ChannelModel: h_{at}, h_{al}, h_{pl}, h_{af}
DetectionType $\in$ {IM/DD, Heterodyne}
Ensure: Joint Outage Probability, P_J
Compute channel gain: $H \leftarrow h_{at} \cdot h_{al} \cdot h_{pl} \cdot h_{af}$
if DetectionType == Heterodyne
  $\gamma \leftarrow (N_1 \cdot \beta \cdot H) \cdot \overline{\gamma}$
else if DetectionType == IM/DD **then**
  $\gamma \leftarrow (N_1 \cdot \beta \cdot H)^2 \cdot \overline{\gamma}$
end if
if ProtocolType == TS **then**
  $Q \leftarrow \tau\eta^2 P_t^r \beta^2 \mathcal{N}^2 \mathcal{H}^2$
  $R \leftarrow (1-\tau) \cdot \log_2(1+\gamma)$
  $E \leftarrow (1-\tau)\mathcal{N}P_e + P_c$ **then**
else if ProtocolType == ES **then**
  $Q \leftarrow \eta^2 P_t^r \rho^2 \mathcal{N}_2^2 \mathcal{H}^2$
  $R \leftarrow \log_2\left[1 + (\mathcal{N}_1\beta\mathcal{H})^r \overline{\gamma}\right]$
  $E \leftarrow P_{RIS}^{ACT} + \mathcal{N}_2(\rho P_e + P_{DC}) + P_{rx}$
else if ProtocolType == PS **then**
  $Q \leftarrow \eta^2 \zeta^r P_t^r \beta^2 \mathcal{N}^2 \mathcal{H}^2$
  $R \leftarrow \log_2\left[1 + ((1-\zeta)\mathcal{N}\beta\mathcal{H})^r \overline{\gamma}\right]$
  $E \leftarrow \mathcal{N}P_e + P_c$
end if
Compute outage probabilities:
$P_{J1} \leftarrow \Pr[Q \le E]$ ▷using channel CDF $F_{H_I}(Z_1)$
$P_{J2} \leftarrow \Pr[R \le \log_2(1+\gamma_{\text{th}})]$ ▷using channel CDF $F_H(Z_2)$
Compute joint outage probability:
$P_J \leftarrow P_{J1} + P_{J2} - P_{J1} \cdot P_{J2}$
return P_J

VII. Results and Discussion

This study investigates the performance of the ORIS-assisted SWIPT-UOWC system on a unified channel model that considers the thermocline gradient and air bubble-induced underwater turbulence in addition to the impact of pointing errors, path loss, and AOA fluctuations. The match between the results of the analytical model with the Monte Carlo simulation of 10^6 realizations, according to the parameters listed in Table I, validates channel performance of outage probability, ergodic capacity, and joint probability of outage of

TABLE I
SYSTEM PARAMETERS

Parameter	Value	Parameter	Value
λ	520 nm	$< \mathrm{T} >$	15 °C
$< \mathrm{S} >$	20 ppt	C_c	0.03 g/m^3
χ_T	10^{-7} K^2/s	ε	10^{-4} m^2/s^3
H	-2 °.ppt^{-1}	σ_s	$1 \times r_a$
L	20 m	q_H	0.7
F_0	∞	D_G, W_0	2 cm, 2 cm
γ_{th}	0 dB	w_b	$3 \times r_a$
σ_0	12 mrad	θ_{FOV}	50 mrad

TABLE II
THE WGG DISTRIBUTION PARAMETERS UNDER $\mathrm{G}_T = 0.2$ °C/CM AND $\mathrm{G}_s = 0.2$ (G/L CM)

R_A (L/min)	σ_I^2	[ω, k, ϖ,a,b,c]
5	0.3571	[0.2676, 2.1737, 0.3609 72.4188, 1×10^{-6}, 0.2974]
2	0.6725	[0.4200,1.6400,0.2870 69.8487,1.0248×10^{-6}, 0.2974]
5	1.7670	[0.3150, 2.6702, 3.1768 0.1755, 0.5155,4.3411]

energy harvesting and data rate of (*i*) ES, (*ii*) PS, and (*iii*) TS power transfer methods. Hence, the results focus on examining the impact of two criteria. The first criterion is the scintillation index σ_I^2 values when the temperature gradient and the salinity gradient are 0.2°C/cm, 0.2 g/L cm, respectively, and the airflow rates are 2 L/min and 5 L/min, as given in Table II. The second criterion is the number of ORIS elements (*i.e.*, $\mathcal{N}$), which is set to 10, 20, 40 and 80 elements unless stated otherwise.

Fig. 2 shows analytical (based on Eq.(Eq. (19))) and simulated OP against the average SNR IM/DD detection for scintillation index σ_I^2 of 0.3571, 0.6725 and 1.7670 and number of passive elements N = 60. The results show an excellent match between analytical and simulation results, verifying the validity of analysis. As expected, OP values decrease with decreasing scintillation index values. This result is consistent with the findings of the experimental study in [30], which concluded that increasing the thermocline gradient introduces strong turbulence, and the airflow rate obstructs the communication link and increases the outage probability.

After investigating the OP for various scintillation index σ_I^2 values and fixed $\mathcal{N}$ in Fig. 2, Fig. 3 illustrates OP versus average SNR values for various number of passive elements, while the scintillation index σ_I^2 equals 1.7670. As expected, the OP values decrease when the ORIS has a large number of passive elements. As shown in the figure, a twofold increase in the number of passive elements (*i.e.*, $\mathcal{N}$), leads to a consistent

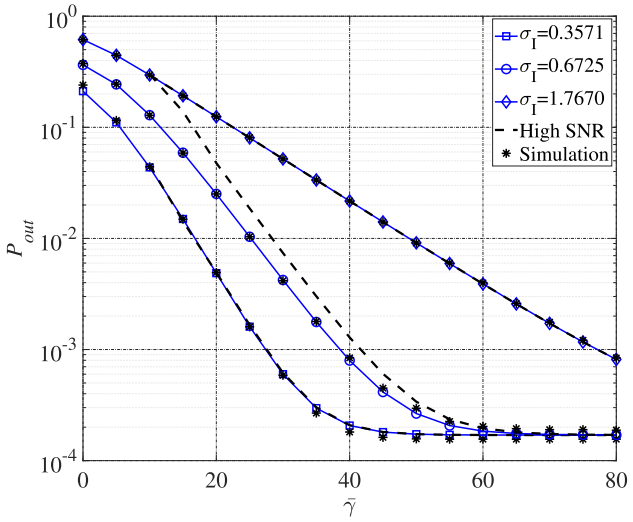

Fig. 2. OP versus the average SNR, using IM/DD detection for various scintillation index σ_I^2 values and number of passive elements $\mathcal{N} = 60$.

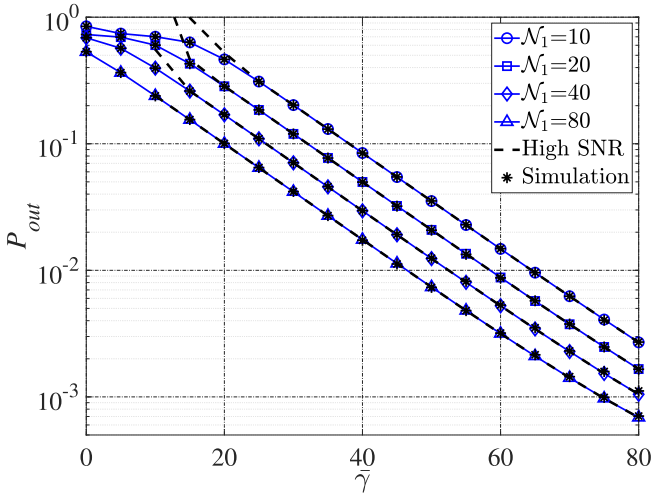

Fig. 3. OP versus the average SNR, using IM/DD detection for various numbers of passive elements and $\sigma_I^2 = 1.7670$.

reduction in the outage probability values and hence a uniform performance gain achieved with each doubling.

Fig. 4 illustrates the BER performance of M-ary modulation schemes M-PSK and M-QAM with heterodyne detection. The purpose of the modulation comparison is not limited to illustrating the expected degradation of higher–order constellations, but to quantify their sensitivity under the proposed unified underwater channel model. This analysis provides practical design guidance for selecting modulation schemes in RIS–assisted SWIPT UOWC systems operating under severe turbulence and attenuation conditions. The analysis includes $M = [2, 8, 16, 64]$ for the former and $M = [16, 64]$ for the latter. The tightness between the results of simulation, asymptotic expression and analytical expression validates the performance expectations, particularly the enhanced BER values that M-QAM offers compared to M-PSK for the same values of $M = 16$ and $M = 64$.

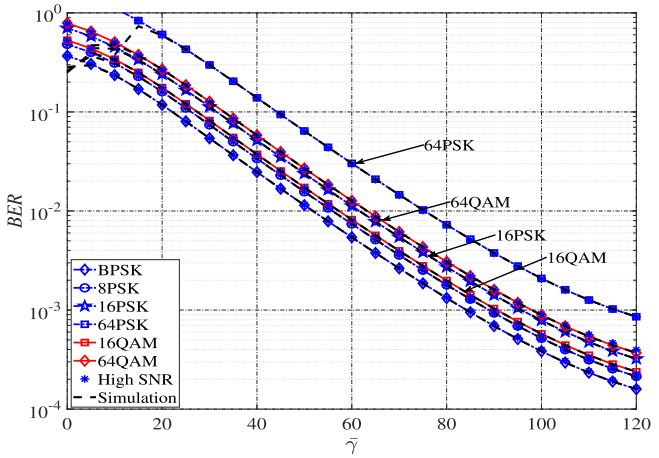

Fig. 4. Average BER versus the average SNR for M-PSK and M-QAM with heterodyne detection, when $\sigma_s = 3 \times r_a$, $\mathcal{N}_1 = 60$ and $\sigma_I^2 = 1.7670$.

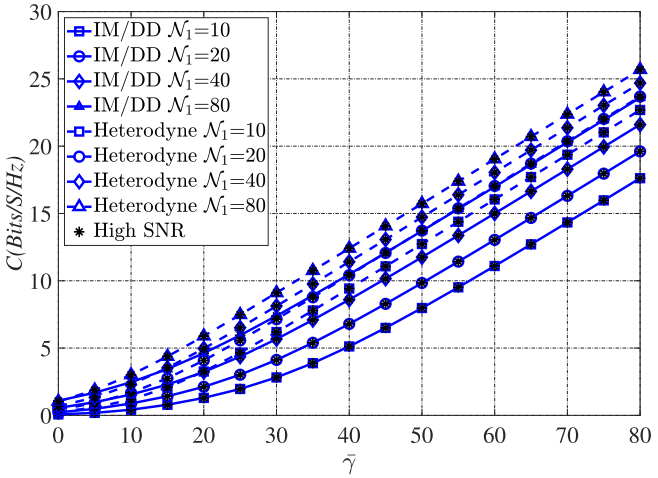

Fig. 6. Ergodic capacity versus the average SNR, in case of IM/DD and heterodyne detection, for various number of ORIS elements and $\sigma_I^2 = 1.7670$.

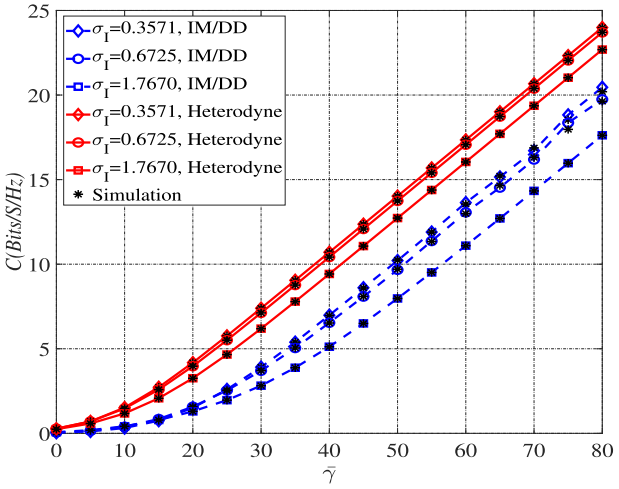

Fig. 5. Ergodic capacity versus the average SNR, in case of IM/DD and heterodyne detection, for various scintillation index σ_I^2 values and fixed ORIS elements (*i.e.*, $\mathcal{N}_1 = 60$).

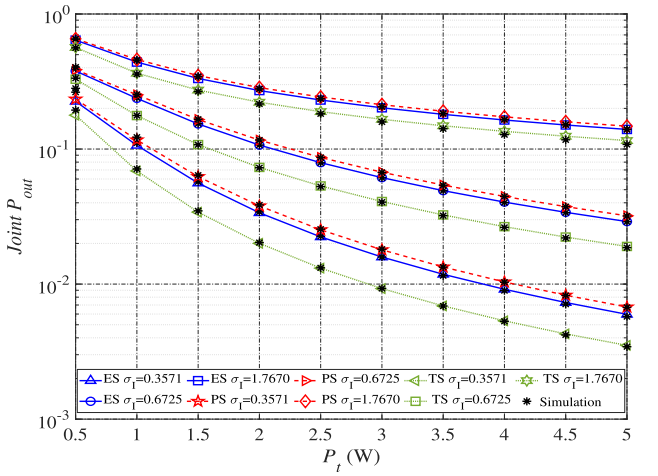

Fig. 7. Energy harvesting and data rate OP of ES, PS and TS power transfer methods versus transmitted power values using IM/DD detection, assuming $\mathcal{N} = 60$ for PS and TS, $\mathcal{N}_1 = 22$ and $\mathcal{N}_2 = 38$ for ES, $\zeta = 1$, and $\tau = 1$.

The ergodic capacity of the ORIS-assisted SWIPT-UOWC system under the proposed unified channel model is provided in Fig. 5 for $\sigma_I^2 = 0.3571$, 0.6725 and 1.7670 and $\mathcal{N}_1 = 60$ elements for IM/DD and heterodyne detection. The analytical results match the simulation results; validating the accuracy of the proposed channel model to predict the ergodic capacity of the system. In addition, the results are consistent with the theoretical expectations, *i.e.* increasing the value of σ_I^2, which indicates stronger turbulence, reduces the channel capacity for IM/DD and heterodyne detection schemes, with the latter achieving superior performance. It is worth noting that the purpose of this comparison is not merely to indicate the superiority of heterodyne detection, but to quantify the performance gap under the proposed unified underwater channel conditions and RIS-assisted SWIPT protocols, thereby providing practical design insight for complexity–performance trade-offs.

Similarly, in Fig. 6 the ergodic capacity of the system is provided when $\mathcal{N}_1 = [10, 20, 40, 80]$ and $\sigma_I^2 = 1.7670$ for IM/DD and heterodyne detection. As the figure illustrates, using more ORIS elements enhances the channel capacity. Furthermore, as was observed in Fig. 3 in the OP case, doubling the number of passive elements, $\mathcal{N}_1$, results in a uniform and predictable performance gain achieved with each doubling.

Fig. 7 illustrates the joint energy harvesting and data rate OP for ES, PS and TS power transfer methods as a function of transmitted power when $\bar{\gamma} = 50$ dB, $\mathcal{N} = 60$ for PS and TS, and $\mathcal{N}_1 = 22$ and $\mathcal{N}_2 = 38$ for ES under the fairness power consumption condition of active and passive ORIS elements. σ_I^2 is set to 1.7670, and $\zeta = \tau = 1$. The tight agreement between the analytical and simulation results confirms the accuracy of the analysis presented in Section VI. As it can also be observed that TS power transfer method achieves lower outage probability those achieved by ES and PS power transfer methods when the same transmitted power is used. However, all methods require a high transmitted power value of at least 4 W to achieve an OP performance below 10^{-2}. Therefore, to study the joint OP, the transmitted power value is set to 4 W.

In Fig. 8, the joint energy harvesting and data rate operation performance of the ES, PS, and TS methods is presented

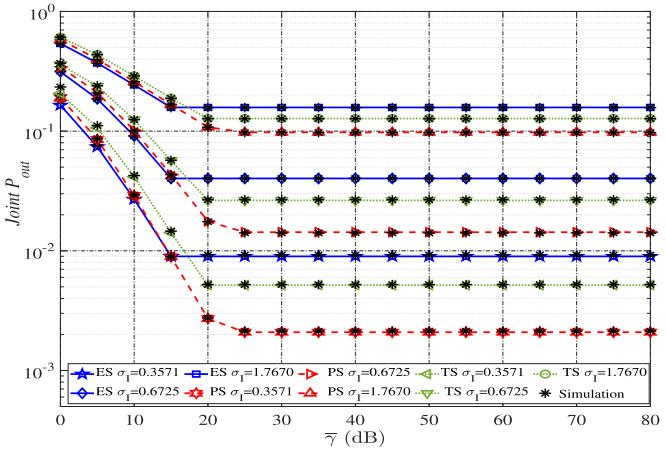

Fig. 8. Energy harvesting and data rate OP of ES, PS and TS power transfer methods versus average SNR values using IM/DD detection, assuming $\mathcal{N} = 60$ for PS and TS, $\mathcal{N}_1 = 22$ and $\mathcal{N}_2 = 38$ for ES, $\zeta = 1$, and $\tau = 1$.

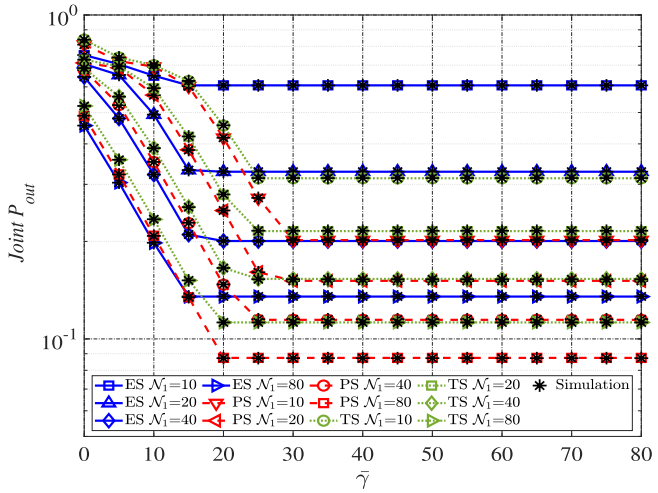

Fig. 9. Energy harvesting and data rate OP in ES, PS and TS method versus average SNR values using IM/DD detection, assuming $\mathcal{N} = 60$ for PS and TS, $\mathcal{N}_1 = 22$ and $\mathcal{N}_2 = 38$ for ES, $\zeta = 1$, and $\tau = 1$.

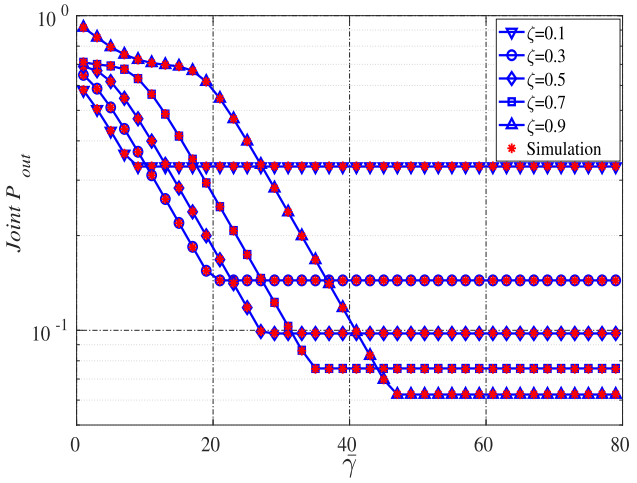

Fig. 10. Energy harvesting and data rate OP of PS protocol versus the average SNR, for various values of ζ using IM/DD detection.

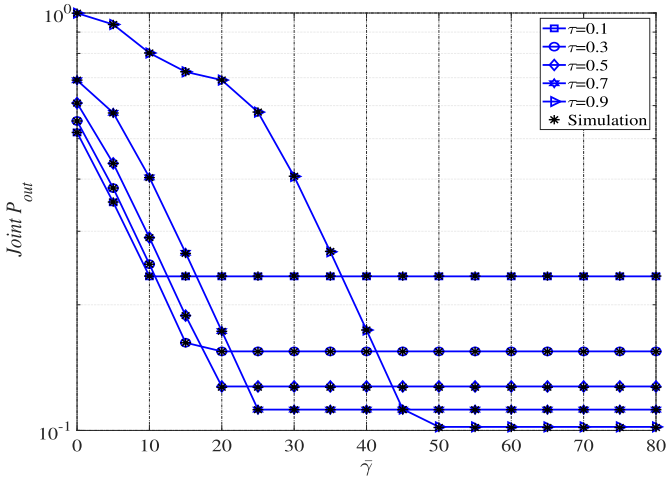

Fig. 11. Energy harvesting and data rate OP of TS method versus the average SNR values, for various values of τ and using IM/DD detection, assuming $\mathcal{N} = 60$.

against average SNR values for IM/DD detection. Both ζ and τ are set to 1. Generally, at low SNR values, the OP performance is affected by the data rate OP, which corresponds to the second term of Eq. (33). As SNR increases and surpasses 20 dB, the performance stabilizes at a constant value that reflects the OP of energy harvesting (the first term of Eq. (33), as it is independent of the average SNR values. Therefore, beyond $\overline{\gamma} = 20$ dB, further increases in SNR do not improve the joint OP. Additionally, the figure illustrates that at low SNR values, the ES method delivers better operation performance compared to the PS and TS methods. Conversely, the PS method exhibits the lowest operation performance when the SNR exceeds 20 dB. A similar trend is observed in Fig. 9, which depicts the joint energy harvesting and data rate operation performance of the ES, PS, and TS power transfer methods against average SNR values for $\sigma_I^2 = 1.7670$, with $\mathcal{N} = [10, 20, 40, 80]$ elements when a constant ratio between $\mathcal{N}_1$ and $\mathcal{N}_2$ of 36:63 for EH and IT, respectively, and considering the fairness power consumption of ORIS elements also using IM/DD detection. As anticipated, increasing the number of ORIS elements results in reduced operation performance, with a noticeable performance improvement for the PS method when SNR values exceed 30 dB.

In Fig. 10, the joint energy harvesting and data rate OP of the PS power transfer method versus average SNR values is examined for various values of ζ using IM/DD detection. $\mathcal{N}_1$ is set to 60, $\sigma_I^2 = 1.7670$, and the transmitted power equals 4 W. While using $\zeta = 0.1$ achieves relatively low OP values at lower SNR, the OP values plateau at 0.33 after $\overline{\gamma} = 9$ dB. In contrast, using larger values, *e.g.*, $\zeta = 0.9$, enhances the OP performance to 0.06 for SNR values exceeding 47 dB. Hence, selecting the operational ζ value as a design factor depends on the expected average SNR of the system.

Fig. 11 shows the joint energy harvesting and data rate OP of TS power transfer method versus average SNR values for various values of τ using IM/DD detection, when $\mathcal{N}_1 = 60$, $\sigma_I^2 = 1.7670$, and the transmitted power equals 4 W. Similar to the scenario discussed in Fig. 10, while smaller values of τ yield lower OP outcomes at low SNR, the OP values stabilizes at 0.23 as SNR exceeds 10 dB. Conversely, larger τ values

lead to improved OP performance at high SNR. For example, when $\tau = 0.9$, the OP reaches a steady state at 0.1 when SNR exceeds 50 dB.

From the derived closed-form expressions and the obtained plots, several key design insights can be extracted. The SINR increases linearly with the reflection coefficient β_r and the number of RIS elements $\mathcal{N}$, confirming that larger number of RIS apertures significantly enhances link reliability. However, the improvement saturates at high $\mathcal{N}$ due to turbulence-induced decorrelation among elements. The OP decreases with increasing transmitted optical power P_t and reflection efficiency, while it increases with turbulence variance and attenuation coefficient, which jointly determine the effective channel gain. These analytical relations indicate that optimizing $\mathcal{N}$, β, and beam alignment parameters provides an efficient means to minimize the OP without excessive transmit power or active element usage.

VIII. Conclusion

This paper investigates a unified channel model for UOWC systems, affected by multiple additive attenuation losses that may occur in a realistic environment. In this scenario, we consider an ORIS-assisted SWIPT-UOWC system for simultaneous EH and IT at the Rx. Different transmission protocols have been investigated, such as PS, TS, and ES, respectively exploiting the allocation of power, time slots, and ORIS elements. For PS and TS, we consider the ORIS works with all passive elements, while in ES mode the ORIS is able to activate passive and active elements simultaneously. After deriving the closed-form expression of the unified PDF of SNR, under the assumption of IM/DD or heterodyne detection, we present the joint OPs for EH and IT in the case of PS, TS, and ES. Simulation results highlight the superiority of heterodyne detection over IM/DD, as it achieves higher performance. Then, using higher number of ORIS elements provides an improvement of performance. Finally, comparing different transmission protocols, we observe that ES is more effective for low average SNR, while PS and TS show a better behavior for increasing values of SNR. In this study, we considered that a line-of-sight link between Tx-ORIS-Rx exists. The impact of the link geometry and the optimal position of the ORIS on the channel model is an interesting future research direction.

Appendix A
Conditioned PDF

The PDF of pointing error $f_{h_{pl}}(h_{pl})$ given in Eq. (6) over deviation angle θ_d can be deduced by

$$f_{h_{pl}|\theta_d}(h_{pl}) = \frac{\eta_s^2}{2\pi q_H} \int_{-\pi}^{\pi} \frac{h_{pl}^{\eta_s^2\xi(\varphi)-1}}{(A_0\cos\theta_d)^{\eta_s^2\xi(\varphi)}} d\varphi. \tag{A.1}$$

Then, inserting Eqs. (4) and (A.1) into Eq. (13), we obtain

$$\begin{aligned} f_{h_{ag}|\theta_d}(h_{ag}) = \frac{\eta_s^2}{2\pi q_H} \int_{-\pi}^{\pi} \frac{h_{ag}^{\eta_s^2\xi(\varphi)-1}}{(A_0 h_{al}\cos\theta_d)^{\eta_s^2\xi(\varphi)}} \mathrm{d}\varphi \\ \times \left[\frac{\omega k}{\varpi^k} \int_{\Delta_1}^{\infty} h_{at}^{k-\eta_s^2\xi(\varphi)-1} e^{-\frac{h_{at}^k}{\varpi^k}} \mathrm{d}h_{at} \right. \\ \left. + \frac{(1-\omega)c}{b^{ac}\Gamma(a)} \int_{\Delta_1}^{\infty} h_{at}^{ac-\eta_s^2\xi(\varphi)-1} e^{-\frac{h_{at}^c}{\varpi^c}} \mathrm{d}h_{at} \right]. \end{aligned} \tag{A.2}$$

Applying [44, Eq.(3.381-9)], Eq. (A.2) becomes as

$$\begin{aligned} f_{h_{ag}|\theta_d}(h_{ag}) = \frac{\eta_s^2}{2\pi q_H} \int_{-\pi}^{\pi} \frac{h_{ag}^{\eta_s^2\xi(\varphi)-1}}{(A_0 h_{al}\cos\theta_d)^{\eta_s^2\xi(\varphi)}} \mathrm{d}\varphi \\ \times \left[\frac{\omega}{\varpi^{\eta_s^2\xi(\varphi)}} \Gamma\left(\frac{k-\eta_s^2\xi(\varphi)}{k}, \left(\frac{\Delta_1}{\varpi}\right)^k \right) \right. \\ \left. + \frac{(1-\omega)}{b^{\eta_s^2\xi(\varphi)}\Gamma(a)} \Gamma\left(\frac{ac-\eta_s^2\xi(\varphi)}{c}, \left(\frac{\Delta_1}{b}\right)^c \right) \right], \end{aligned} \tag{A.3}$$

where $\Gamma(a,b)$ is the upper incomplete gamma function.

Appendix B
Channel PDF Derivations

Inserting Eqs. (7) and (A.3) into Eq. (14), we obtain Eq. (B.1), as shown at the bottom of the page, and using small angle approximation, *i.e.*, $\cos\theta_d \approx 1$, it becomes

$$\begin{aligned} f_{\mathcal{H}}(\mathcal{H}) = \frac{\omega\eta_s^2}{2\pi q_H} \int_{-\pi}^{\pi} \frac{\mathcal{H}^{\eta_s^2\xi(\varphi)-1}}{(A_0 h_{al}\varpi)^{\eta_s^2\xi(\varphi)}} \\ \times \Gamma\left(\frac{k-\eta_s^2\xi(\varphi)}{k}, \left(\frac{\Delta_4}{\varpi}\right)^k \right) \mathrm{d}\varphi \mathcal{I}_1 + \frac{(1-\omega)\eta_s^2}{2\pi q_H\Gamma(a)} \end{aligned}$$

$$\begin{aligned} f_{\mathcal{H}}(\mathcal{H}) = \frac{\omega\eta_s^2}{2\pi q_H} \int_{-\pi}^{\pi} \frac{\mathcal{H}^{\eta_s^2\xi(\varphi)-1}}{(A_0 h_{al}\varpi)^{\eta_s^2\xi(\varphi)}} \mathrm{d}\varphi \int_0^{\theta_{FOV}} \frac{\theta_d}{\sigma_0^2(\cos\theta_d)^{\eta_s^2\xi(\varphi)}} \Gamma\left(\frac{k-\eta_s^2\xi(\varphi)}{k}, \left(\frac{\Delta_4}{\varpi\cos\theta_d}\right)^k \right) \exp\left(-\frac{\theta_d^2}{2\sigma_0^2}\right) \mathrm{d}\theta_d \\ + \frac{(1-\omega)\eta_s^2}{2\pi q_H\Gamma(a)} \int_{-\pi}^{\pi} \frac{\mathcal{H}^{\eta_s^2\xi(\varphi)-1}}{(A_0 h_{al} b)^{\eta_s^2\xi(\varphi)}} \mathrm{d}\varphi \int_0^{\theta_{FOV}} \frac{\theta_d}{\sigma_0^2(\cos\theta_d)^{\eta_s^2\xi(\varphi)}} \Gamma\left(\frac{ac-\eta_s^2\xi(\varphi)}{c}, \left(\frac{\Delta_4}{b\cos\theta_d}\right)^c \right) \exp\left(-\frac{\theta_d^2}{2\sigma_0^2}\right) \mathrm{d}\theta_d \\ + \delta(\mathcal{H}) \int_{\theta_{FOV}}^{\infty} \frac{\theta_d}{\sigma_0^2} \exp\left(-\frac{\theta_d^2}{2\sigma_0^2}\right) \mathrm{d}\theta_d, \end{aligned} \tag{B.1}$$

$$\times \int_{-\pi}^{\pi} \frac{\mathcal{H}^{\eta_s^2\xi(\varphi)-1}}{(A_0 h_{al} b)^{\eta_s^2\xi(\varphi)}} \Gamma\left(\frac{ac-\eta_s^2\xi(\varphi)}{c}, \left(\frac{\Delta_4}{b}\right)^c\right) \mathrm{d}\varphi \times \mathcal{I}_1 + \delta(\mathcal{H})\mathcal{I}_2, \tag{B.2}$$

with $\mathcal{I}_1 = \int_0^{\theta_{FOV}} \frac{\theta_d}{\sigma_0^2} \exp\left(-\frac{\theta_d^2}{2\sigma_0^2}\right) \mathrm{d}\theta_d$ and $\mathcal{I}_2 = \int_{\theta_{FOV}}^{\infty} \frac{\theta_d}{\sigma_0^2} \exp\left(-\frac{\theta_d^2}{2\sigma_0^2}\right) \mathrm{d}\theta_d$. Applying Eqs. (3.381-8) and (3.381-9) of [44] to $\mathcal{I}_1$ and $\mathcal{I}_2$ and inserting the results into Eq. (B.2), the PDF of channel will be obtained as in Eq. (15).

Appendix C
Channel CDF Derivations

Inserting Eq. (17) into $F_\gamma(\gamma) = \int_0^\gamma f_\gamma(x)\mathrm{d}x$, we have

$$\begin{aligned} F_\gamma(\gamma) &= \frac{\omega\eta_s^2\Delta_3}{2\pi q_H r} \int_{-\pi}^{\pi} \mathrm{d}\varphi \int_0^\gamma \frac{1}{x} G_{1,2}^{2,0}\left(\frac{(x/\overline{\gamma})^{\frac{k}{r}}}{(\varpi\Delta_5)^k} \middle| \begin{matrix} \frac{k+\eta_s^2\xi(\varphi)}{k} \\ \frac{\eta_s^2\xi(\varphi)}{k}, 1 \end{matrix}\right) \mathrm{d}x \\ &+ \frac{(1-\omega)\eta_s^2\Delta_3}{2\pi q_H \Gamma(a) r} \int_{-\pi}^{\pi} \mathrm{d}\varphi \int_0^\gamma \frac{1}{x} G_{1,2}^{2,0}\left(\frac{(x/\overline{\gamma})^{\frac{c}{r}}}{(b\Delta_5)^c} \middle| \begin{matrix} \frac{c+\eta_s^2\xi(\varphi)}{c} \\ \frac{\eta_s^2\xi(\varphi)}{c}, a \end{matrix}\right) \mathrm{d}x \\ &+ \Delta_2 \int_0^\gamma \frac{x^{\frac{1}{r}-1}}{r\overline{\gamma}^{\frac{1}{r}}\mathcal{N}_1\beta} \delta\left(\frac{x^{\frac{1}{r}}}{\overline{\gamma}^{\frac{1}{r}}\mathcal{N}_1\beta}\right) \mathrm{d}x. \end{aligned} \tag{C.1}$$

To solve the first and second integrals in Eq. (C.1), we utilize the parameter conversions as $t = x^{k/r}$ and $t = x^{c/r}$, respectively. Then, we apply Eq. (26) of [45] to both integrals. To solve the last integral in Eq. (C.1), we apply the parameter conversion as $t = \frac{(\gamma/\overline{\gamma})^{(1/r)}}{\mathcal{N}_1\beta}$. Then, the CDF of the SNR can be obtained as given in Eq. (18).

Appendix D
Average BER Derivations

Inserting the PDF of the SNR given in Eq. (17) into Eq. (20), we obtain the error probability as expressed in Eq. (D.1), as shown at the bottom of the page.

According to Eq. (06.06.26.0005.01) of [36], the upper incomplete gamma function in both $\mathcal{I}_3$ and $\mathcal{I}_4$ can be written in terms of Meijer-G function as $\Gamma(p, q_s\gamma) = G_{1,2}^{2,0}\left(q_s\gamma \middle| \begin{matrix} 1 \\ 0, p \end{matrix}\right)$. Also, $\mathcal{I}_3$ and $\mathcal{I}_4$ can be solved by inserting this expression and applying Eq. (07.34.21.0012.01) of [36]. To solve $\mathcal{I}_5$, we apply the parameter conversion $t = \frac{(\gamma/\overline{\gamma})^{(1/r)}}{\mathcal{N}_1\beta}$ and use the property $\int_0^\infty \delta(x)f(x) = f(0)$. Finally, combining all solutions will lead to the average BER expression given in Eq. (22).

Appendix E
Channel Capacity Derivations

Inserting the PDF of SNR given in Eq. (17) into Eq. (21), we get the expression of channel capacity as in Eq. (E.1), as show at the top of the next page. According to Eq. (11) of [45], the term $\ln(1+c_r\gamma)$ in both $\mathcal{I}_6$ and $\mathcal{I}_7$ can be written through Meijer-G function as $\ln(1+c_r\gamma) = G_{2,2}^{1,2}\left(c_r\gamma \middle| \begin{matrix} 1,1 \\ 1,0 \end{matrix}\right)$, and both integrals can be solved by using Eq. (07.34.21.0012.01) of [36]. To solve $\mathcal{I}_8$, we use $t = \frac{\gamma^{\frac{1}{r}}}{\overline{\gamma}^{\frac{1}{r}}\mathcal{N}_1\beta}$, then using $\int_0^\infty f(t)\delta(t)dt = f(0)$ will lead $\mathcal{I}_8 = 0$. Combining integral solutions for $\mathcal{I}_6$, $\mathcal{I}_7$ and $\mathcal{I}_8$ in Eq. (E.1), the ergodic channel capacity will be obtained as given in Eq. (31).

Appendix F
High SNR Derivations

According to [46, pp.9], an H-function reduces to Meijer-G function as

$$H_{p,q}^{m,n}\left(z \middle| \begin{matrix} (a_1,P),..,(a_p,P) \\ (b_1,P),..,(b_q,P) \end{matrix}\right) = \frac{1}{P} G_{p,q}^{m,n}\left(z^{\frac{1}{P}} \middle| \begin{matrix} a_1,..,a_p \\ b_1,..,b_q \end{matrix}\right). \tag{F.1}$$

Also, the asymptotic expansion of H-function for small arguments is expressed in [47, pp.19] by

$$H_{p,q}^{m,n}\left[z \middle| \begin{matrix} (a_i,\alpha_i)_{1,p} \\ (b_i,\beta_i)_{1,q} \end{matrix}\right] = \sum_{j=1}^{m} h_j^* z^{\frac{b_j}{\beta_j}}, \quad z \to 0 \tag{F.2}$$

while h_j^* coefficients are

$$h_j^* = \frac{1}{\beta_j} \frac{\prod_{\substack{i=1 \\ i\neq j}}^{m} \Gamma\left(b_i - b_j\frac{\beta_i}{\beta_j}\right) \prod_{i=1}^{n} \Gamma\left(1-a_i+b_j\frac{\alpha_i}{\beta_j}\right)}{\prod_{i=n+1}^{p} \Gamma\left(a_i - b_j\frac{\alpha_i}{\beta_j}\right) \prod_{i=m+1}^{q} \Gamma\left(1-b_i+b_j\frac{\beta_i}{\beta_j}\right)}. \tag{F.3}$$

Appendix G
WGG Channel CDF Derivations

Any probability of $P_r(\mathcal{H} < \mathcal{Z})$ can be found by using the CDF of the channel as

$$P_r(\mathcal{H} < \mathcal{Z}) = F_{\mathcal{H}}(\mathcal{Z}) = \int_0^{\mathcal{Z}} f_{\mathcal{H}}(\mathcal{H}) d\mathcal{H}. \tag{G.1}$$

$$\begin{aligned} P_e = &\underbrace{\frac{\delta\omega\eta_s^2\Delta_3}{4\pi q_H r\Gamma(p)} \sum_{s=1}^{n_x} \int_{-\pi}^{\pi} \mathrm{d}\varphi \int_0^\infty \frac{1}{\gamma}\Gamma(p,q_s\gamma) G_{1,2}^{2,0}\left(\frac{(\gamma/\overline{\gamma})^{\frac{k}{r}}}{(\varpi\Delta_5)^k} \middle| \begin{matrix} \frac{k+\eta_s^2\xi(\varphi)}{k} \\ \frac{\eta_s^2\xi(\varphi)}{k}, 1 \end{matrix}\right) \mathrm{d}\gamma}_{\mathcal{I}_3} + \frac{\delta(1-\omega)\eta_s^2\Delta_3}{4\pi q_H r\Gamma(p)\Gamma(a)} \sum_{s=1}^{n_x} \int_{-\pi}^{\pi} \mathrm{d}\varphi \\ &\times \underbrace{\int_0^\infty \frac{1}{\gamma}\Gamma(p,q_s\gamma) G_{1,2}^{2,0}\left(\frac{(\gamma/\overline{\gamma})^{\frac{c}{r}}}{(b\Delta_5)^c} \middle| \begin{matrix} \frac{c+\eta_s^2\xi(\varphi)}{c} \\ \frac{\eta_s^2\xi(\varphi)}{c}, a \end{matrix}\right) \mathrm{d}\gamma}_{\mathcal{I}_4} + \frac{\delta\Delta_2}{2\Gamma(p)} \sum_{s=1}^{n_x} \underbrace{\int_0^\infty \Gamma(p,q_s\gamma) \frac{\gamma^{\frac{1}{r}-1}}{r\overline{\gamma}^{\frac{1}{r}}\mathcal{N}_1\beta} \left(\frac{\gamma^{\frac{1}{r}}}{\overline{\gamma}^{\frac{1}{r}}\mathcal{N}_1\beta}\right) \mathrm{d}\gamma}_{\mathcal{I}_5}. \end{aligned} \tag{D.1}$$

$$\overline{C} = \frac{\omega\eta_s^2\Delta_3}{2\pi q_H r\ln(2)}\int_{-\pi}^{\pi}\mathrm{d}\varphi\underbrace{\int_0^{\infty}\frac{1}{\gamma}\ln(1+c_r\gamma)G_{1,2}^{2,0}\left(\frac{(\gamma/\overline{\gamma})^{\frac{k}{r}}}{(\varpi\Delta_5)^k}\middle|\begin{matrix}\frac{k+\eta_s^2\xi(\varphi)}{k}\\ \frac{\eta_s^2\xi(\varphi)}{k},1\end{matrix}\right)\mathrm{d}\gamma}_{\mathcal{I}_6} + \frac{(1-\omega)\eta_s^2\Delta_3}{2\pi q_H\Gamma(a)r\ln(2)}\int_{-\pi}^{\pi}\mathrm{d}\varphi$$
$$\times\underbrace{\int_0^{\infty}\frac{1}{\gamma}\ln(1+c_r\gamma)G_{1,2}^{2,0}\left(\frac{(\gamma/\overline{\gamma})^{\frac{c}{r}}}{(b\Delta_5)^c}\middle|\begin{matrix}\frac{c+\eta_s^2\xi(\varphi)}{c}\\ \frac{\eta_s^2\xi(\varphi)}{c},a\end{matrix}\right)\mathrm{d}\gamma}_{\mathcal{I}_7} + \frac{\Delta_2}{\ln(2)}\underbrace{\int_0^{\infty}\ln(1+c_r\gamma)\frac{\gamma^{\frac{1}{r}-1}}{r\overline{\gamma}^{\frac{1}{r}}\mathcal{N}_1\beta}\delta\left(\frac{\gamma^{\frac{1}{r}}}{\overline{\gamma}^{\frac{1}{r}}\mathcal{N}_1\beta}\right)\mathrm{d}\gamma}_{\mathcal{I}_8}. \tag{E.1}$$

Using the PDF given in Eq. (15) and expressing upper incomplete gamma function with Meijer-G function with the help of Eq. (06.06.26.0005.01) of [36] and then, applying the procedures given in APPENDIX-C, the CDF of the channel becomes

$$F_{\mathcal{H}}(\mathcal{Z}) = \frac{\omega\eta_s^2\Delta_3}{2\pi q_H k}\int_{-\pi}^{\pi}G_{2,3}^{2,1}\left(\frac{\mathcal{Z}^k}{\Delta_6^k}\middle|\begin{matrix}1,\frac{k+\eta_s^2\xi(\varphi)}{k}\\ \frac{\eta_s^2\xi(\varphi)}{k},1,0\end{matrix}\right)\mathrm{d}\varphi$$
$$+\frac{(1-\omega)\eta_s^2\Delta_3}{2\pi q_H\Gamma(a)c}\int_{-\pi}^{\pi}G_{2,3}^{2,1}\left(\frac{\mathcal{Z}^c}{\Delta_7^c}\middle|\begin{matrix}1,\frac{c+\eta_s^2\xi(\varphi)}{c}\\ \frac{\eta_s^2\xi(\varphi)}{c},a,0\end{matrix}\right)\mathrm{d}\varphi$$
$$+\Delta_2 H(\mathcal{Z}), \tag{G.2}$$

where $\Delta_6 = \varpi A_0 h_{al}$ and $\Delta_7 = bA_0 h_{al}$.

REFERENCES

[1] M. C. Domingo, "An overview of the Internet of Underwater Things," *J. Netw. Comput. Appl.*, vol. 35, no. 6, pp. 1879–1890, 2012. [Online]. Available: https://www.sciencedirect.com/science/article/pii/S1084804512001646

[2] M. Jouhari, K. Ibrahimi, H. Tembine, and J. Ben-Othman, "Underwater wireless sensor networks: A survey on enabling technologies, localization protocols, and Internet of Underwater Things," *IEEE Access*, vol. 7, pp. 96879–96899, 2019.

[3] M. Eshaghi and R. Rashidzadeh, "An energy harvesting solution for IoT devices in 5G networks," in *Proc. IEEE Can. Conf. Electr. Comput. Eng. (CCECE)*, Aug. 2020, pp. 1–4.

[4] T. D. Ponnimbaduge Perera, D. N. K. Jayakody, S. K. Sharma, S. Chatzinotas, and J. Li, "Simultaneous wireless information and power transfer (SWIPT): Recent advances and future challenges," *IEEE Commun. Surveys Tuts.*, vol. 20, no. 1, pp. 264–302, 1st Quart., 2018.

[5] M. A. Hossain, R. Md Noor, K.-L.-A. Yau, I. Ahmedy, and S. S. Anjum, "A survey on simultaneous wireless information and power transfer with cooperative relay and future challenges," *IEEE Access*, vol. 7, pp. 19166–19198, 2019.

[6] N. Sharma, S. Gautam, S. Chatzinotas, and B. Ottersten, "Integrating multiple RIS for enhanced SWIPT-IoT performance: Optimization strategies," *IEEE Access*, vol. 12, pp. 182841–182855, 2024.

[7] Q. Wu and R. Zhang, "Towards smart and reconfigurable environment: Intelligent reflecting surface aided wireless network," *IEEE Commun. Mag.*, vol. 58, no. 1, pp. 106–112, Jan. 2020.

[8] P. Ramezani, B. Lyu, and A. Jamalipour, "Toward RIS-enhanced integrated terrestrial/non-terrestrial connectivity in 6G," *IEEE Netw.*, vol. 37, no. 3, pp. 178–185, May 2023.

[9] W. Long, R. Chen, M. Moretti, W. Zhang, and J. Li, "A promising technology for 6G wireless networks: Intelligent reflecting surface," *J. Commun. Inf. Netw.*, vol. 6, no. 1, pp. 1–16, Mar. 2021.

[10] Q. Wu and R. Zhang, "Weighted sum power maximization for intelligent reflecting surface aided SWIPT," *IEEE Wireless Commun. Lett.*, vol. 9, no. 5, pp. 586–590, May 2020.

[11] C. Pan et al., "Intelligent reflecting surface aided MIMO broadcasting for simultaneous wireless information and power transfer," *IEEE J. Sel. Areas Commun.*, vol. 38, no. 8, pp. 1719–1734, Aug. 2020.

[12] H. Abumarshoud et al., "LiFi through reconfigurable intelligent surfaces: A new frontier for 6G?," *IEEE Vehicular Technology Magazine*, vol. 17, no. 1, pp. 37–46, Jan. 2022.

[13] R. P. Naik and W.-Y. Chung, "Evaluation of reconfigurable intelligent surface-assisted underwater wireless optical communication system," *J. Lightw. Technol.*, vol. 40, no. 13, pp. 4257–4267, Mar. 31, 2022.

[14] A. R. Ndjiongue, T. M. N. Ngatched, and O. A. Dobre, "On the capacity of RIS-assisted intensity-modulation optical channels," *IEEE Commun. Lett.*, vol. 26, no. 2, pp. 389–393, Feb. 2022.

[15] Q. Zhang, D.-W. Yue, and X.-Y. Xu, "Performance analysis of reconfigurable intelligent surface-assisted underwater wireless optical communication systems," *IEEE Photon. J.*, vol. 16, no. 4, pp. 1–14, Aug. 2024.

[16] Y. Luo, L. Pu, J. Diao, C. Liu, and A. Song, "Underwater acoustic reconfigurable intelligent surfaces: From principle to practice," *IEEE Commun. Standards Mag.*, early access, May 28, 2025, doi: 10.1109/MCOMSTD.2025.3572257.

[17] S. Kisseleff, S. Chatzinotas, and B. Ottersten, "Reconfigurable intelligent surfaces in challenging environments: Underwater, underground, industrial and disaster," *IEEE Access*, vol. 9, pp. 150214–150233, 2021.

[18] M. Uysal, S. Ghasvarianjahromi, M. Karbalayghareh, P. D. Diamantoulakis, G. K. Karagiannidis, and S. M. Sait, "SLIPT for underwater visible light communications: Performance analysis and optimization," *IEEE Trans. Wireless Commun.*, vol. 20, no. 10, pp. 6715–6728, Oct. 2021.

[19] C. Edemen, M. T. Altabbaa, and M. Uysal, "Channel modeling of reconfigurable intelligent surface-aided underwater acoustic communication system," in *Proc. 32nd Signal Process. Commun. Appl. Conf. (SIU)*, May 2024, pp. 1–3.

[20] A. P. Kamali, S. N. Prathyusha, T. Parveen, and A. Priya, "Challenges encountered with reconfigurable intelligent surfaces (RIS) in underwater communication," in *Proc. 3rd Int. Conf. Electr., Electron., Inf. Commun. Technol. (ICEEICT)*, Jul. 2024, pp. 1–5.

[21] X. Luo, L. Yang, and A.-A.-A. Boulogeorgos, "Performance assessment of active-RIS-assisted mixed RF-UAC systems," *IEEE Trans. Veh. Technol.*, vol. 74, no. 3, pp. 4569–4581, Mar. 2025.

[22] Z. Wei, Z. Wei, J. Fang, J. Pan, L. Wang, and Y. Dong, "Impulse response modeling and dynamic analysis for SIMO UOWC systems enhanced by RIS-equipped UUVs," *IEEE Trans. Veh. Technol.*, vol. 73, no. 2, pp. 1540–1553, Feb. 2024.

[23] J. Song, X. Liu, W. Luo, and J. Zhang, "Performance analysis of STAR-RIS assisted UWOC-RF systems with NOMA," in *Proc. 9th Int. Conf. Intell. Comput. Signal Process. (ICSP)*, Apr. 2024, pp. 1316–1320.

[24] L. B. Kumar, R. P. Naik, P. Krishnan, A. A. B. Raj, A. K. Majumdar, and W.-Y. Chung, "RIS assisted triple-hop RF-FSO convergent with UWOC system," *IEEE Access*, vol. 10, pp. 66564–66575, 2022.

[25] Z. Gan, M. Cox, and Y. Dong, "On RIS-aided NLOS underwater wireless optical communication systems," in *Proc. Photon. Electromagn. Res. Symp. (PIERS)*, Apr. 2024, pp. 1–7.

[26] Y. Dong, Z. Chen, Z. Song, Y. Chen, and X. Zhang, "Reconfigurable intelligent surface transmission for data importance classification in underwater acoustic networks with energy holes," in *Proc. IEEE Int. Conf. Signal Process., Commun. Comput. (ICSPCC)*, Nov. 2023, pp. 1–4.

[27] E. E. Elsayed et al., "Coding techniques for diversity enhancement of dense wavelength division multiplexing MIMO-FSO fault protection protocols systems over atmospheric turbulence channels," *IET Optoelectronics*, vol. 18, nos. 1–2, pp. 11–31, Feb. 2024. [Online]. Available: https://ietresearch.onlinelibrary.wiley.com/doi/abs/10.1049/ote2.12111

[28] M. Singh, E. E. Elsayed, M. Alayedi, M. H. Aly, and S. A. Abd El-Mottaleb, "Performance analysis in spectral-amplitude-coding-optical-code-division-multiple-access using identity column shift matrix code in free space optical transmission systems," *Opt. Quantum Electron.*, vol. 56, no. 5, Mar. 2024.

[29] Y. Ata, X. Yi, Y. Li, X. Tao, and A. M. Vegni, "A unified channel model for IRS-aided underwater OWC with combined attenuation losses," *IEEE J. Sel. Areas Commun.*, vol. 43, no. 5, pp. 1552–1567, May 2025.
[30] H. Qiu, Z. Huang, J. Xu, W. Zhai, Y. Gao, and Y. Ji, "Unified statistical thermocline channel model for underwater wireless optical communication," *Opt. Lett.*, vol. 48, no. 3, pp. 636–639, 2023.
[31] A. Morel and L. Prieur, "Analysis of variations in ocean color 1," *Limnology Oceanogr.*, vol. 22, no. 4, pp. 709–722, 1977.
[32] V. I. Haltrin, "Chlorophyll-based model of seawater optical properties," *Appl. Opt.*, vol. 38, no. 33, pp. 6826–6832, 1999.
[33] B. Zhou, P. Wang, T. Cao, G. Li, S. Li, and P. Yang, "Performance analysis of AUV-carried RISs-aided multihop UWOC convergent with RF MRC systems over WGG oceanic turbulence," *Veh. Commun.*, vol. 45, Feb. 2024, Art. no. 100722.
[34] W. Gappmair, S. Hranilovic, and E. Leitgeb, "OOK performance for terrestrial FSO links in turbulent atmosphere with pointing errors modeled by Hoyt distributions," *IEEE Commun. Lett.*, vol. 15, no. 8, pp. 875–877, Aug. 2011.
[35] H. Safi, A. Dargahi, J. Cheng, and M. Safari, "Analytical channel model and link design optimization for ground-to-HAP free-space optical communications," *J. Lightw. Technol.*, vol. 38, no. 18, pp. 5036–5047, May 22, 2020.
[36] *The Wolfram Functions Site*. [Online]. Available: https://functions.wolfram.com
[37] E. Zedini, H. M. Oubei, A. Kammoun, M. Hamdi, B. S. Ooi, and M.-S. Alouini, "Unified statistical channel model for turbulence-induced fading in underwater wireless optical communication systems," *IEEE Trans. Commun.*, vol. 67, no. 4, pp. 2893–2907, Apr. 2019.
[38] E. Zedini, H. Soury, and M.-S. Alouini, "Dual-hop FSO transmission systems over gamma–gamma turbulence with pointing errors," *IEEE Trans. Wireless Commun.*, vol. 16, no. 2, pp. 784–796, Feb. 2017.
[39] I. S. Ansari, F. Yilmaz, and M.-S. Alouini, "Performance analysis of free-space optical links over Málaga ($\mathcal{M}$) turbulence channels with pointing errors," *IEEE Trans. Wireless Commun.*, vol. 15, no. 1, pp. 91–102, Jan. 2016.
[40] Y. Ata, E. Zedini, A. M. Vegni, and M.-S. Alouini, "Reflect-and-amplify: A novel SWIPT technique through hybrid Active/Passive RIS," *IEEE Internet Things J.*, vol. 12, no. 12, pp. 22073–22089, Jun. 2025.
[41] M.-M. Zhao, Q. Wu, M.-J. Zhao, and R. Zhang, "Intelligent reflecting surface enhanced wireless networks: two-timescale beamforming optimization," *IEEE Trans. Wireless Commun.*, vol. 20, no. 1, pp. 2–17, Jan. 2021.
[42] Z. Yang and Y. Zhang, "Beamforming optimization for RIS-aided SWIPT in cell-free MIMO networks," *China Commun.*, vol. 18, no. 9, pp. 175–191, Sep. 2021.
[43] C. Huang, A. Zappone, G. C. Alexandropoulos, M. Debbah, and C. Yuen, "Reconfigurable intelligent surfaces for energy efficiency in wireless communication," *IEEE Trans. Wireless Commun.*, vol. 18, no. 8, pp. 4157–4170, Aug. 2019.
[44] I. S. Gradshteyn and I. M. Ryzhik, *Table of Integrals, Series, and Products*. New York, NY, USA: Academic, 2014.
[45] V. S. Adamchik and O. I. Marichev, "The algorithm for calculating integrals of hypergeometric type functions and its realization in REDUCE system," in *Proc. Int. Symp. Symbolic Algebr. Comput.*, Jul. 1990, pp. 212–224.
[46] C. A. Coelho and B. C. Arnold, *Finite Form Representations for Meijer G and Fox H Functions*. Cham, Switzerland: Springer, 2019.
[47] A. A. Kilbas, *H-Transforms: Theory and Applications*. Boca Raton, FL, USA: CRC Press, 2004.